POLITECNICO DI TORINO

Master's Degree in Nanotechnologies for ICTs

Master's Degree Thesis

Delayed Differential Equation Analysis of Harmonic Mode Locking in Quantum Dot Ring Lasers

Supervisor

Prof. Paolo BARDELLA

Candidate

Mathias TAPINETTO

April 2024

Contents

Abstract

The demand for ultra-fast and broad-band communication has opened up an active research topic to improve telecommunication performance. In particular, in the last 25 years, the requested bandwidth has doubled every 18 months with an increase of the data rates that are expected to grow beyond 10 Gb/s in the near future. In this sense, sub-terahertz spectrum (0.1 THz - 0.3 THz) has become more and more attractive. However, the designing of electronic solutions (e.g. mixers and amplifiers) which couple efficiency and reasonable costs represent a non trivial problem to be overcome. The easiest solution is to take advantage of the optical generation of pulses which can be converted in the electrical domain by means of a photoantenna. To generate pulses having a repetition rate in the window of interest, many techniques are possible, but the most used one is based on mode-locking. In this technique, the phase between adjacent modes is fixed so that a resonant phenomenon rises. More specifically, a direct consequence of the phase-locking is the destructively interference of all the modes at periodic interval of time so that pulses could be generated. In particular, in order to reach high values of repetition rates, harmonic mode locking can be exploited. This technique relies on the presence of two or more optical pulses traveling along the cavity. In our case, we deal with multi-section structures, characterised by the alternation of absorption regions (reversely biased) and gain sections (forward biased). The extraction of a high frequency signal can happen in any SA thanks to the aforementioned antenna. Ideally, frequencies above 200 GHz can be achieved but stable circulation of pulses in harmonic mode-locking regime must be assured. To ameliorate and enhance the generation of optical pulses, Quantum Dots (QD) can be inserted in the active material. This quantum objects are structures confined in all directions for which discrete confined energy levels rises. In particular they have the peculiar characteristic to assemble spontaneously on a substrate so that they can be easily integrated in opto-electronic devices. In this thesis, the possibility to embed QDs in a ring cavity laser exploiting the harmonic mode locking regime was studied. Among the effects gained by the laser in this case, there are high temperature stability and ultrafast carrier dynamics. Of course QD suffers also of some drawbacks in particular the production cost and the incompatibility with CMOS technology. In addition, the quantum dynamic processes involved in QD must be considered to detail a complete theory of such structures and simulate their behavior in a cavity, increasing the complexity of the analysis. The goal of this thesis

is to design and simulate the beahvior of a QD based ring laser operating in harmonic ML regime. For this study, I used a MATLAB algorithm based on the delayed differential equations approach to successfully simulate the dynamic processes inside the ring cavity involving opto-electronic variables. Indeed, my particular contribution consisted in taking advantage of the pre-existing mathematical model to simulate QD-based ring cavity lasers able to sustain repetition frequencies above 150 GHz. Actually, the simulated structure implements the so-called quantum dots in a well, a structure in which the quantum confinement is regularly reduced to pass from a non-confined structure to the proper said QD.

Chapter 1

Introduction

1.1 General basis about Laser Theory

The basis for the development of a more complex theory on the dynamics of lasers is the comprehension of the principles that rule it. Such principles are here exposed to form the basis of the multi-section delayed differential equations model, which is the main feature of this thesis.

1.1.1 The Stimulated Emission

The acronym LASER was coined by Gordon Gould in 1959 and means Light Amplification by Stimulated Emission of Radiation. In order to understand what the stimulated emission is, the elementary electron-photon interaction illustrated in Figures 1.1,1.2, 1.3 must be considered.

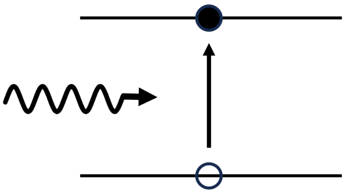

Figure 1.1: Absorption

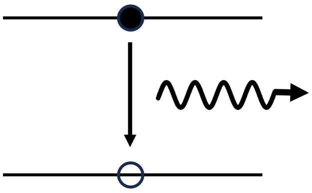

Figure 1.2: Spontaneous Emission

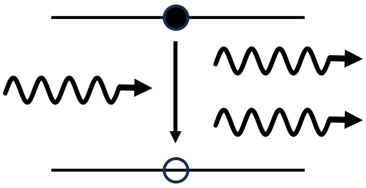

Figure 1.3: Stimulated Emission

The three main interactions that occur between atoms and photons are absorption, spontaneous emission, and stimulated emission. In absorption, one photon from the radiation field transfers its energy to an electron, which is promoted to a higher quantum level. In order to be effective, the energy provided must be equal to the difference of the two energetic levels, so if the photon has an energy of $\hbar\omega$, and E_n, E_m are the energies associated with the two confined levels, it is verified that $\hbar\omega = E_n - E_m$. In spontaneous emission, an electron spontaneously falls into a less energetic quantum state, losing energy $\hbar\omega = E_n - E_m$. Stimulated emission occurs only when an electromagnetic wave influences an exited atom by inducing the emission of a photon in addition to the incoming one. Therefore, if the atom is excited, the stimulated emission gives rise to a net gain that amplifies the radiation. The condition under which the electronic population is in a more energetic state than the equilibrium one is called Inversion of Population. As a direct consequence of what stated above, there are three main requirements that must be fulfilled in order to constitute a laser:

- an electrical or optical pump to achieve the inversion of population;
- an active material which provides the electronic population in order to amplificate the radiation. In the case of laser diodes, which are the ones analyzed in this thesis, it is a semiconductor.
- a cavity in which the power is trapped in order to give rise to a resonance phenomenon. A small portion of this power will be extracted.

In fact, what is present in a laser is not only the amplification of the electromagnetic radiation but also a resonance phenomenon implemented by the interaction between the emitted light and the amplified medium.

Threshold current

In order to have a net gain, the stimulated emission must prevail on the spontaneous one. Let us consider having a flux of injected electrons that will constitute a current I whose charges will undergo the stimulated emission. The density of charges in time could be described by the following differential equation:

$$\frac{\mathrm{d}N}{\mathrm{d}t} = G_{\text{gen}} - R_{\text{rec}} \tag{1.1}$$

where G_{gen} and R_{rec} are the generation and the recombination rates. The number of electrons per second is $\frac{\eta_i I}{q}$ and this is the only contribution to the generation term, therefore:

$$G_{\text{gen}} = \frac{\eta_i I}{qV} \tag{1.2}$$

In the previous equation, η_i is the so called injection efficiency and it is the fraction of the current that generates charges in the active region. The recombination rate will be the sum of various contributions, such as spontaneous emission, nonradiative emission, stimulated emission, Auger recombination, and, finally, a leakage recombination. A simplified approach consists of adopting the so-called ABC model for the recombination so that:

$$R_{rec} = AN + BN^2 + CN^3 + R_{st} \tag{1.3}$$

In particular, the linear term in N takes into account the non radiative phenomena, the quadratic term models the Spontaneous recombination, and the cubic term models the Auger recombinations. The term R_{st} stands for the stimulated recombination rate. Physically, what happens is that the injected charges will accumulate, increasing the gain until a threshold condition is reached. Above this threshold, the stimulated emission prevails and equation (1.1) could be rewritten as:

$$\frac{\mathrm{d}N}{\mathrm{d}t} = \frac{\eta_i I}{qV} - (AN + BN^2 + CN^3) - v_g g N_p \tag{1.4}$$

where v_g is the group velocity, g is the gain, and N_p is the density of photons. Regarding the temporal evolution of this kind of particles, it must be considered that the volume of the cavity that they occupy V_p is much larger than the volume of the cavity itself V. For this reason, it is useful to define a confinement factor:

$$\Gamma = \frac{V}{V_p} \tag{1.5}$$

It can be demonstrated that the temporal evolution of photonic density can be described by:

$$\frac{\mathrm{d}N_p}{\mathrm{d}t} = \Gamma R_{st} + \Gamma \beta_{sp} R_{sp} - \frac{N_p}{\tau_p} \tag{1.6}$$

where β_{sp} is the spontaneous emission coefficient and τ_p is the the photon lifetime. Physically, when the threshold is reached, the stimulated emission term increases. A dynamical equilibrium is reached so that the charge density and the gain are clamped, and the emitted power increase. In particular, it can be shown that the output power could be described by:

$$P = \begin{cases} \eta_d \frac{\hbar\omega}{q}(I - I_{th}), & I > I_{th} \\ \eta_r \eta_i \frac{\alpha_m}{\langle\alpha_i\rangle + \alpha_m} \frac{\hbar\omega}{q} \beta_{sp} I & I < I_{th}. \end{cases} \tag{1.7}$$

where α_i is called internal modal loss and α_m is called mirror loss (a parameter related essentially to geometrical properties of the cavity). On the other hand, the gain could be written as:

$$g = \begin{cases} G_0 \ln \frac{N}{N_{tr}} & N_{tr} < N < N_{th} \\ G_0 \ln \frac{N_{th}}{N_{tr}} & N > N_{th} \end{cases} \tag{1.8}$$

where the attention has been focused on the region of positive gain, $g \geq 0$, G_0 is a constant N_{tr} is called transparency density and

$$N_{th} = N_{tr} e^{\frac{\langle \alpha_i \rangle + \alpha_m}{\Gamma G_0}} \tag{1.9}$$

The general trend of g and N could be depicted as in Figure 1.4.

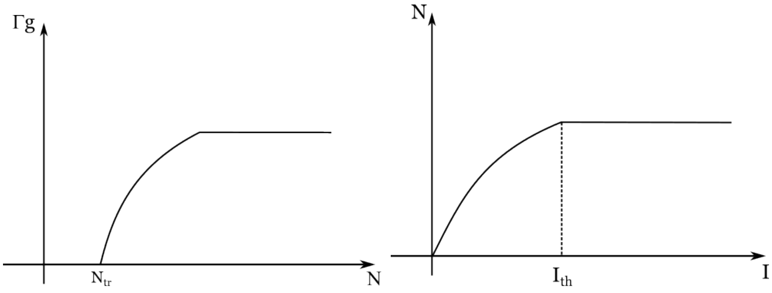

Figure 1.4: Trends for gain and carriers density

1.1.2 Quantum Confinement

Until the 1980s, the laser diodes were made with bulky materials but unwanted effects, such as large losses, were relevant. To avoid these problems, a confinement of both carriers and photons was introduced. The confinement of carriers, constituted by electrons and holes, is achieved by designing a heterostructure in which the active layer (the one that exploits the stimulated emission and amplification) is placed between two materials with a higher bandgap. This is obtained because of the discontinuities of the valence and conduction band. Instead, the optical confinement is achieved by tailoring the active layer in such a way that its refractive index is higher than that of the surrounding materials. Moreover, the confinement could also occur in more dimensions, also meeting the need of more and more scaled devices. More precisely, the confinement in one direction is obtained when the material size is lower, or at least comparable, than the so-called De Broglie wavelength:

$$\lambda_B = \frac{h}{p} = \frac{h}{mv} \tag{1.10}$$

If the bulk material is confined in one dimension, a 2D structure is obtained. This structure is called a Quantum Well. Confining one more dimension, a 1D structure, named Quantum Wire, is described. Also, a 0D structure is achievable and is referred to as a Quantum Dot.

1.1.3 Electronic Structure

The confinement along one direction will affect the electronic and optical properties exhibited by the material. Let us suppose to consider a crystalline (periodic) material whose lattice constants in the three dimensions are, respectively, L_x,L_y,L_z. What is relevant is the so-called density of states.

Definition 1 *The 3D Density of States (3D-DOS) is the number of electron (hole) states per unit of energy per unit of volume of the crystal.*

$$D(E) = \frac{1}{V}\frac{\mathrm{d}N}{\mathrm{d}E} \tag{1.11}$$

where dN is the number of quantum states present in the energy range between E and $E + dE$. In order to calculate it, it is necessary to know which wavevectors are allowed in such a system. Solving the Schrodinger equation for a periodic lattice, it is demonstrable that the eigenvectors are plain waves of the form:

$$\psi = \frac{1}{\sqrt{A}} e^{i(k_x x + k_y y + k_z z)} \tag{1.12}$$

where A is a normalization constant. Imposing the Periodic Boundary Condition, proper of a crystal, it is easy to write:

$$\psi(x + L_x, y, z) = \psi(x, y, z) \tag{1.13}$$

$$\frac{1}{\sqrt{A}} e^{i(k_x x + k_x L_x + k_y y + k_z z)} = \frac{1}{\sqrt{A}} e^{i(k_x x + k_y y + k_z z)} \tag{1.14}$$

which is equivalent to say that:

$$e^{ik_x L_x} = 1 \Rightarrow k_x = \frac{2\pi}{L_x} n_1 \tag{1.15}$$

where n_1 is an integer number. Imposing the periodicity on the other dimensions, it is straightforward to find that:

$$k_y = \frac{2\pi}{L_y} n_2 \tag{1.16}$$

$$k_z = \frac{2\pi}{L_z} n_3 \tag{1.17}$$

This results allows to define a new space, called k-space, defined as the Cartesian product of $k_x \times k_y \times k_z$ (see Figure 1.5). Now it is possible to calculate the number of states N dividing the volume of a sphere of radius k (i.e. the total number of states that has k as a wavevector) by that of a single state cube.

$$N = 2 \cdot \frac{\frac{4}{3}\pi k^3}{\left(\frac{2\pi}{L_x}\right)\left(\frac{2\pi}{L_y}\right)\left(\frac{2\pi}{L_z}\right)} = \frac{V^3 k^3}{3\pi^2} \tag{1.18}$$

In the previous equation, a factor 2 is introduced to consider the spin degeneracy and it was considered that $V = L_x L_y L_z$. Recalling that

$$E = \frac{\hbar^2 k^2}{2m} \Rightarrow k = \sqrt{\frac{2mE}{\hbar}} \tag{1.19}$$

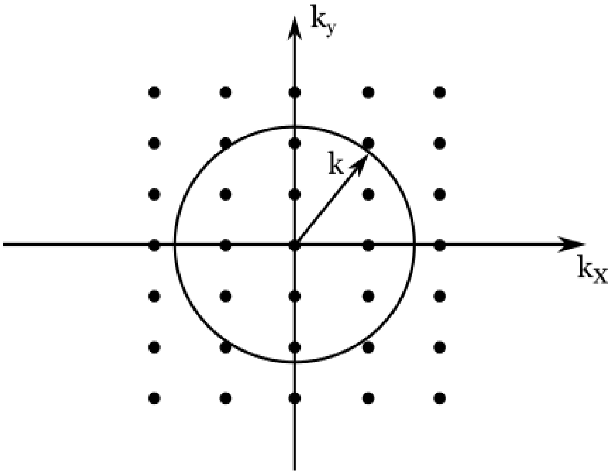

Figure 1.5: Projection of the 3D k-space in 2D

the final expression of N and $\frac{\mathrm{d}N}{\mathrm{d}E}$ could be easely found:

$$N = \frac{V}{3\pi^2}\left(\frac{2mE}{\hbar^2}\right)^{\frac{3}{2}} \tag{1.20}$$

$$\frac{\mathrm{d}N}{\mathrm{d}E} = \frac{V}{2\pi^2}\left(\frac{2m}{\hbar^2}\right)^{\frac{3}{2}}\sqrt{E} \tag{1.21}$$

Therefore,

$$D = \frac{1}{2\pi^2}\left(\frac{2m}{\hbar^2}\right)^{\frac{3}{2}}\sqrt{E} \tag{1.22}$$

The density of states at any particular energy is the sum over all the bands:

$$\rho^{3D} = \sum_{i=1}^{N} D \cdot \theta(E - E_i) \tag{1.23}$$

where θ is the step function:

$$\theta(E - E_i) = \begin{cases} 0, & E < E_i \\ 1, & E > E_i \end{cases} \tag{1.24}$$

Finally, for the conduction and valence bands, the total density of states is:

$$\rho^{3D}_{CB} = \frac{1}{2\pi^2}\left(\frac{2m}{\hbar^2}\right)^{\frac{3}{2}}\sqrt{E - E_C} \tag{1.25}$$

$$\rho^{3D}_{VB} = \frac{1}{2\pi^2}\left(\frac{2m}{\hbar^2}\right)^{\frac{3}{2}}\sqrt{E_V - E} \tag{1.26}$$

Basically, it is found that, if the material is not confined in any direction, the density of states is a continuous function proportional to $\sqrt{E}$. Similarly, the 2D-DOS and 1D-DOS can be defined as:

Definition 2 *The 2D Density of State (2D-DOS) is defined as the number of states that can be occupied by electrons per unit of energy and per unit of surface:*

$$D(E) = \frac{1}{S}\frac{\mathrm{d}N}{\mathrm{d}E} \tag{1.27}$$

Definition 3 *The 1D density of states (1D-DOS) is defined as the number of states that can be occupied by electrons per unit of energy and per unit length:*

$$D(E) = \frac{1}{L}\frac{\mathrm{d}N}{\mathrm{d}E} \tag{1.28}$$

Defining a proper k-space, and repeating the above stated procedure it is possible to demonstrate that:

$$\rho^{2D} = \frac{m}{\pi\hbar^2}\sum_{i=1}^{N}\theta(E-E_i) \tag{1.29}$$

$$\rho^{1D} = \sqrt{\frac{2m}{\hbar^2}}\sum_{i=1}^{N}\frac{1}{\pi\sqrt{E-E_i}}\theta(E-E_i) \tag{1.30}$$

Therefore, if only 2 dimension are free, the density of states is constant; instead, if the carriers are free in only one dimension the density of states is inversely proportional to the $\sqrt{E}$. 2D systems are called Quantum Wells; instead, the 1D ones are named Quantum Wire. When no dimension is free, no k-space could be filled, and all the available states exist at discrete energies. Therefore, the DOS in 0D could be seen as a Dirac delta. Regarding the conduction band it could be written as:

$$D_{0D} = 2\delta(E-E_C) \tag{1.31}$$

As mentioned above, such systems are called Quantum Dots, and all the simulations performed in this thesis will make use of them.

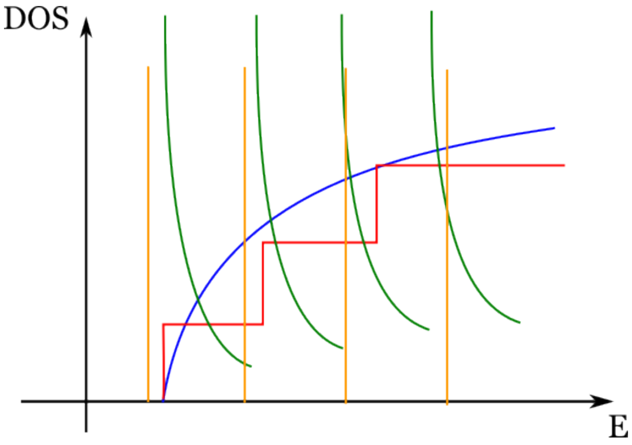

Figure 1.6: 3D DOS in blue, 2D DOS in red, 1D DOS in green, 0D DOS in yellow.

1.2 Broadening of the Quantum Levels in 0D

In the previous paragraph, describing the 0D systems, a uniform spacing between energy levels is assumed. In a more realistic scenario, the weaker localization of the high-order eigenfunctions make these levels become closer to each other. In the following, a system is considered like the one depicted in the Figure 1.7, in which, increasing the energy, there is a transition from the discretized levels of a quantum dot to a continuous band of a 3D system.

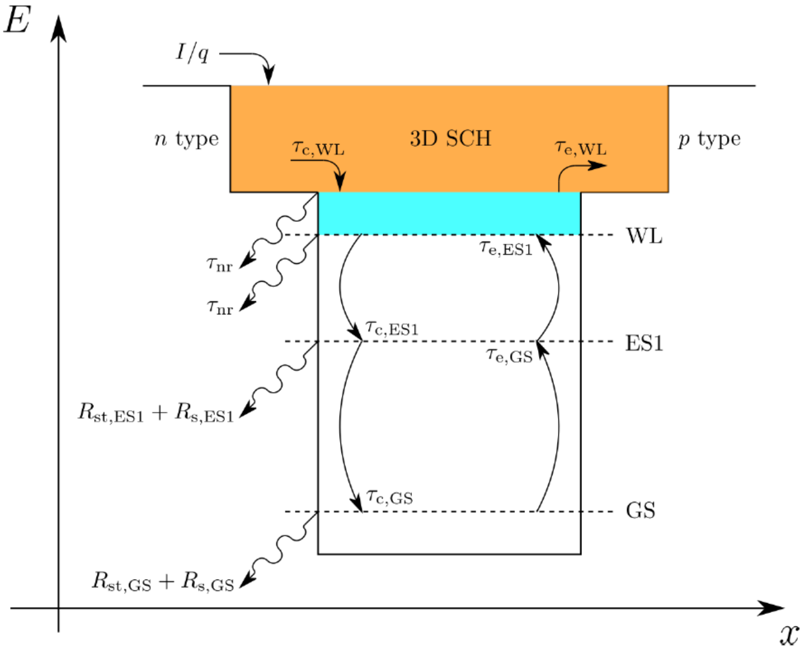

Figure 1.7: Representation of the system considered in this thesis. [19]

Moreover, in the QD fabrication process, there could be fluctuations that could impact the dot sizes. Due to this effect, the confined-state energy levels can be different. In general, the distribution of the confined states energy in the conduction band follows a Gaussian distribution, which for the Ground State (GS) can be expressed as:

$$D_e^{\mathrm{inh}}(E_{e,\mathrm{GS}}) = \frac{1}{\sqrt{\pi}\Delta E^{\mathrm{inh}}_{e,\mathrm{GS}}} e^{-\left(\frac{E_{e,\mathrm{GS}}-E_{e0,\mathrm{GS}}}{\Delta E^{\mathrm{inh}}_{e,\mathrm{GS}}}\right)^2} \tag{1.32}$$

In (1.32), $\Delta E^{\mathrm{inh}}_{e,\mathrm{GS}}$ is the homogeneous broadening, which depends on the size, the strain and the shape of the dot. A similar relation could be written for the holes levels so that a total broadening term could be though as:

$$\Delta E^{\mathrm{inh}}_{\mathrm{GS}} = \Delta E^{\mathrm{inh}}_{e,\mathrm{GS}} + \Delta E^{\mathrm{inh}}_{h,\mathrm{GS}} \tag{1.33}$$

As a result, a more realistic DOS for the 0D system could be drawn by replacing the Dirac Deltas corresponding to the GS and ES1 with two Gaussian distributions with a maximum in correspondence of the ideal energy levels and the ques that overlap between the two maxima (Figure 1.8).

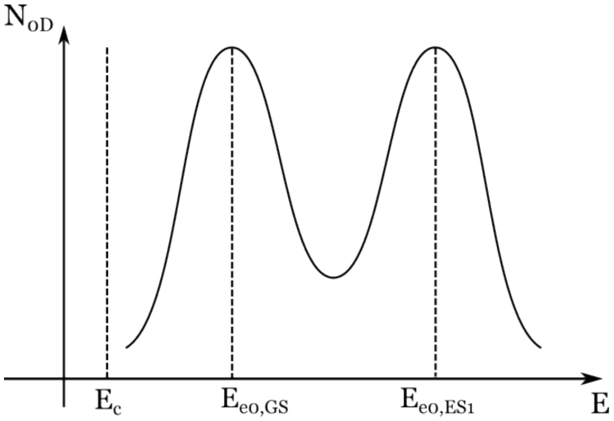

Figure 1.8: 0D DOS for a more realistic system subjected to Inhomogeneous Broadening

In addition, excitons could interact with photons or carriers in the quantum dot or in its proximity, inducing another contribution in the broadening called homogeneous broadening. This event cause the break of the quantum coherence of the electron-hole pairs and could be described by a Lorentzian distribution so that:

$$D^{\text{hom}}_{(e-h)}(E_{\text{ph}}, E_{(e-h),\text{GS}}) = \frac{1}{\pi} \frac{\Delta E^{\text{hom}}_{\text{GS}}}{(E_{\text{ph}} - E_{(e-h),\text{GS}})^2 + (\Delta E^{\text{hom}}_{\text{GS}})^2} \tag{1.34}$$

where $E_{(e-h),GS}$ is the energy separation between the GS levels of electrons and holes and $E_{ph} = \hbar\omega$ is the energy of the photon.

1.3 Aim of this Thesis

Lasers can not only be used for the generation of light in the continuous-wave regime. Indeed, in recent years, the pulsed regime has also become more and more attractive. In particular, in recent decades, the need for ultrafast and broad-band communications has become a serious problem. The requested bandwidth has doubled every 18 months with a subsequent increase in data rates that are expected to grow beyond 10 Gb/s [15, 10]. More specifically, free-space transmission in the sub-terahertz spectrum will imply numerous advantages not only in terms of bandwidth capacity but also of higher directionality and robustness to bad weather events [15, 19]. In addition, the scintillation effects, because of the variation in time of the atmospheric refractive index, are minimized. However, among the drawbacks there is the elevated production cost and the use of bulk technology. [15] In the next chapter, the main technique for generating pulses is analyzed with particular attention to the so-called mode-locking regime. The main scope of this thesis is to simulate the dynamic behavior at high frequency regime of a ring-cavity-based laser that exploits the use of the mode-locking technique with the insertion of QD in the cavity. The specific analysis of the simulated system will be discussed in Chapter 3, where the possibility of reaching a frequency above 100 GHz is demonstrated. Devices that work at tens of gigahertz could already be found in the commercial scenario. The state of the art of quantum dots-based devices is illustrated in Chapter 2. However, the low losses and low dispersion features are coupled with a high production cost, a large power consumption, and a large footprint. To overcome these limitations, other configurations could be exploited. As an example, it is possible to heterodyne two optical sources which emit different wavelengths coupled with a photomixer. In this case, the frequency of the output signals is the difference between the input frequencies. [49] To sum up, femtosecond pulses could meet the need for improvements in the field of telecommunication with several configurations. Moreover, their properties could be improved by introducing quantum dots that not only reduce the footprint of the devices but also improve their optical performances to satisfy the need for transmission in THz wireless telecommunications.

1.3.1 Simulation Model

In performing our simulations, a numerical model is used to describe the mode-locking laser to analyze the dynamic of pulse propagation. Delayed Differential Equations (DDE) are employed to predict the behavior of harmonic and passive mode-locking, whose theory is treated in the next chapter. [52] This allow to reduce the computational cost with respect to other methods, such as Time Domain Traveling Wave one (a model based on the solution of the traveling wave equations in the cavity adopting a finite difference scheme). [53] Instead, the cavity could be divided into multiple sections, so the solution of the DDE in each of them can constitute a self-consistent analysis able to calculate parameters like emitted photocurrent and power. The details about the adopted model are treated in Chapter 3.

Chapter 2

mode-locking Lasers

In the previous chapter, the possibility of using stimulated emission as a source of electromagnetic radiation was discussed, but what is attracting the attention of scientists is not only the production of an optical signal, but also the generation of a train of pulses whose duration is estimated in the range of picoseconds. In this sense, one of the most widely used techniques is the so-called mode-locking, which was first clearly understood by Didomenico in 1964 [13]. From that moment on, many solutions to generate pulses were realized. The first attempts to produce mode-locked pulses relied on the bulky medium employed in solid-state lasers, but the presence of complex optical setup, the high cost of production, and the low efficiency move the research toward more compact solutions based on monolithic semiconductor. In this chapter we will treat first the general theory of the generation of pulses in the mode-locking regime, then we will present the state of the art of the devices that exploit this technique.

2.1 Principles of Mode-Locking Operation

In order to maintain oscillations, the Barkausen criterion must be satisfied. This has an immediate influence on the frequency of the emitted signals. In particular, it can be demonstrated that the emission frequency is fixed by the length of the cavity. The basis for establishing pulses for which the output intensity is no longer constant with time is the operation in multi-mode regimes. The intensity of such a system depends on the phase relation between each mode. If the m modes are supposed to oscillate sinusoidally in the cavity with an identical phase at $t = 0$ with equal amplitude E, the i-th mode will be described by:

$$E_i = E \sin \omega_i t \tag{2.1}$$

Furthermore, let's assume the difference of frequency of the mode $k + i$ will be a fixed number in the form of:

$$\omega_{k+i} - \omega_i = k\Delta\omega \tag{2.2}$$

with k and i integer numbers. At $t = 0$ all the modes are aligned along the same direction; therefore, the resultant amplitude is $E_{TOT} = nE$. After some time Δt, the angular difference between two adjacent modes will be:

$$\theta = \Delta\omega\Delta t \tag{2.3}$$

At a certain time $\Delta\tau$, θ will be equal to $2\pi/m$ and all modes will have the same angular difference between each other. As a result, all modes will interfere destructively. The time at which this phenomenon happens will be:

$$\Delta\tau = \frac{2\pi}{m\Delta\omega} \tag{2.4}$$

On the other hand, when $\theta = 2k\pi$ all the modes will be again aligned and interfere constructively and the total amplitude will again be $E_{TOT} = nE$. This will occur at the time:

$$T = \frac{2k\pi}{\Delta\omega} \tag{2.5}$$

Therefore, with large number of modes m and large $\Delta\omega$, the resultant amplitude will reach the maximum, with a period T. After a time $kT + \Delta\tau$ the amplitude will go to zero very quickly. As a result, what is seen is a periodic train of pulses, each lasting $\Delta\tau$.

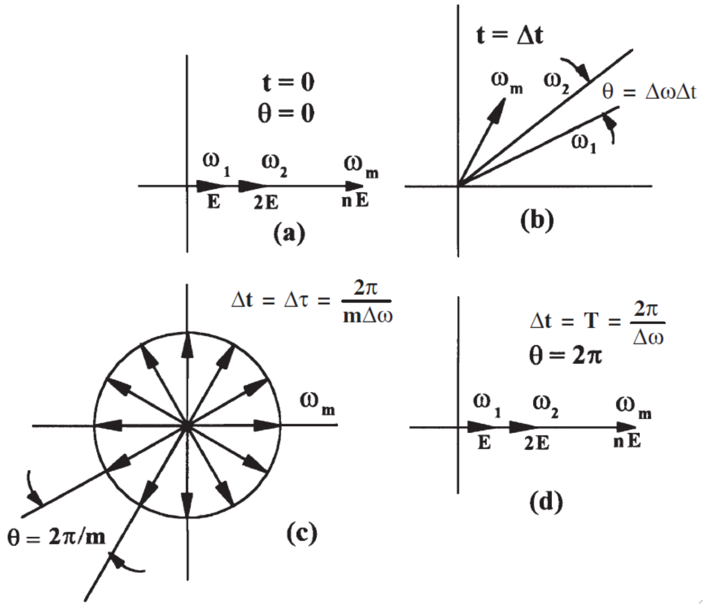

Figure 2.1: Basic operating principle of the mode-locking. The modes are represented at different times and it is clear how they periodically interfere destructively. [54]

A simple illustration of the mechanism illustrated so far is shown in Figure 2.1 where the modes are represented at different times. It is interesting to note that if the cavity length is L and $\Delta\omega = 2\pi c/2L$ then $T = 2L/c$. Of course, in a more complete frame, the number of modes that make up the output field is influenced by the gain of the particular active material used for the laser. The mechanism described so far is known as amplitude modulation mode-locking. In addition, the interaction between adjacent modes causes a beating effect that induces a self-modulation of the carrier density at multiples of the frequency spacing between them. Such modulation implies dynamic variations of the refractive index. This type of modulation originates from interband phenomenon that dominates when the mode spacing is below 1 GHz. They can be ignored for higher frequencies. Self-induced pulses also generate a modulation of the sidebands. Practically, beating between two modes generates injection components, which move the frequencies of other modes. This is a non-ideal effect that arises from the non-perfect locking of the phases. Practically, this effect cannot be completely avoided, but there is a critical value above which the initial angular frequency mismatch is too high to allow mutual locking of the modes.

2.2 Types of mode-locking

The locking of the modes can be reached in several ways. In the following paragraphs, we present the main solutions.

2.2.1 Active Mode-Locking

In order to establish a coupling of modes so that the angular frequency difference between their phases is as constant as possible, one option is to control the injection current using a modulator. The frequency at which this modulation occurs is equal to the round trip of the cavity or a multiple of it. This implies the absence of a passive component which can induce, for example, the Q-switching of the laser (whose detailed treatment lies beyond the aim of this thesis). Furthermore, using an active mode-locking approach, the pulses generated are synchronized with the external clock. In other words, in active mode-locking a device modulates the gain or the losses at which the field is subjected. A kind of modulator that can be used is a Fabry-Pérot modulator in which the modulation depth and the duration of the pulses are achieved by changing the incident modulation power in the modulator [55]. Another approach is to insert an electro-optical modulator. In this particular type of modulator, an external electrical field changes sinusoidally the amplitude of the light in the cavity. When the saturated gain is above the loss, there will be a pulse. A dual mechanism is to induce modulation of the frequency of light inside the cavity. To this aim, an acusto-optic modulator driven by a sinosoidal electric signal can be used. In particular, the limit gain of the material filters the spectral components that are above and below a certain limit. In addition, another possibility is to use another mode-locking laser to switch on and off the pumping source. This last case is referred to as synchronous mode-locking.

2.2.2 Passive Mode-Locking

In passive mode-locking strongly non-linear elements, the saturable absorbers are inserted into the cavity to lock the phase of two subsequent modes. When the pulses travel in these sections, they are reshaped in the form of a narrow peak. In saturable absorbers, the losses are reduced for high intensities of the incoming optical signals, so that low-intensity tails of the signals are absorbed. As a result, only the central portion of the signals is transmitted. With this type of technique, it is possible to obtain pulses with a narrower width. This is particularly true in the case of Quantum Dots-based materials.

2.2.3 Harmonic Mode-Locking

Harmonic mode-locking is achieved when the absorbers saturate not only the pulse traveling in one direction but also another pulse travelling in the opposite direction. Therefore, the obtained repetition rate is twice the fundamental one. The two pulses are forced to collide in the absorbers; for this reason this kind of technique is sometimes referred to as colliding pulse mode-locking. A schematic view of how this kind of regime works is depicted in Figure 2.2. As can be seen in every half-period, two pulses collide and an other pulse is emitted incrementing the repetition frequency.

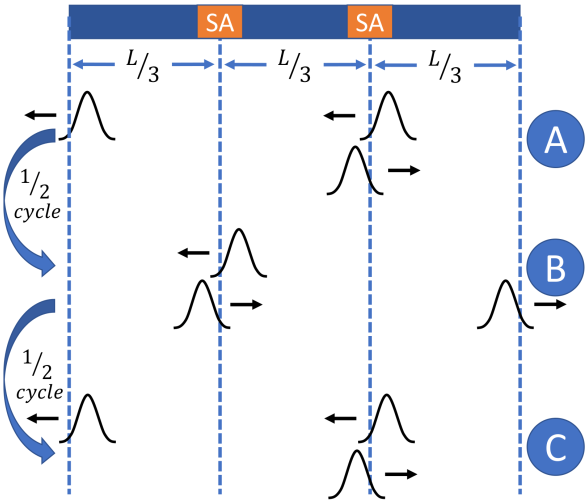

Figure 2.2: Scheme of the physical principle of the harmonic mode-locking [14]

In the case of a ring cavity it is also possible to tailor the cavity itself to allow the circulations of pulses in only one direction. It can be demonstrated that in this case the harmonic mode-locking could also be achieved if there are no collisions of pulses.

2.2.4 Hybrid mode-locking

In Hybrid mode-locking, the modulation is achieved with both passive elements, such as saturable absorbers, and current modulation. This kind of technique allows for more flexibility, but a higher degree of complexity is required. In practice, in most cases reported in the literature, the saturable absorbers are inversely polarized and this voltage is modulated at a frequency f_M close to the frequency of pulse repetition f_P. When their difference $f_M - f_P$ reaches small values, a synchronization between the modulation frequency and the pulse frequency occurs: this process is possible if the frequency separation lies in the locking range. This frequency range has been shown to increase almost linearly with the modulation amplitude [3].

2.2.5 Self Mode-Locking

When a laser, based on a FP cavity, is constituted by a single section and works in a mode-locking regime, it is said to work in self mode-locking. Historically, this was the first solution developed, especially because of the simplicity of the technological realization. However, fluctuation in the fabrication process can lead to an appreciable change in the behavior of the devices so that a trade of between complexity fabrication and robustness is established. Moreover, in such working regime, the pulses may have poor quality and there may be limited tunability. In the literature, such type of mode-locking is referred also as self generated optical frequency comb.

2.3 State of the Art of ML Quantum Dot lasers

The investigation of mode-locking in QD laser for the generation of pulses has been treated as a primary topic in recent years, analyzing the electro-optical characteristics, adapting the model used for simulations, and realizing new structures to optimize the performance also from a technological point of view. The reason beyond this research activity is the expected superior property of quantum dots over not only their bulky counterpart, but also with respect to the quantum well [41]. The most remarkable QD's features are [39, 41]:

- Inhomogeneous broadband gain spectrum.
- Ultra-fast carrier dynamics.
- Large gain and saturable absorber energy ratio.
- Enhanced temperature stability.
- Low linewidth enhancement factor
- Low amplified spontaneous emission level.

Such advantages find application in various fields such as ultrafast spectroscopy, metrology, and imaging. [18] Among the possible employments, QD-based mode-locking devices could answer the demand for high-performance computing and large-scale data centers. [40] This is made possible designing high speed component to meet the exponential growth of data traffic. Moreover, photonic technology is a promising candidate to overcome the physical limitations of copper wires. [41] On the other hand, the main drawback of these devices is their incompatibility with the CMOS technology due to the fact that silicon substrates cannot be used for optoelectronic applications due to the indirect gap of this material. Here we present the state of the art of the QD-based mode-locking lasers established from researches which have been conducted since 2001. We will focus in particular on the most recent results, since from 2018 publications about this topic were much more numerous and focused on telecommunications and transmission of signals.

2.3.1 Early study

The first results were presented by Huang et al. in 2001 in [24]. This first attempt is reported to establish a comparison with a more recent solution exposed in the following. The presented solution relies on quantum dots in a well layer on a n^+ substrate of GaAs. The active regions are two InAs quantum dots in a well layer between which a GaAs barrier layer is inserted. The constituted waveguide is completed by a $Al_{0.7}Ga_{0.3}As$ cladding layers. In this case, a 2-section system is designed with a gain section whose length is 4.73 mm and an SA section of 0.85 mm. Of course, in the gain section, a current is introduced, whereas the SAs experience a reverse bias. The lasing phenomenon involves only the ground state, emitting a wavelength of $\lambda = 1278\,\text{nm}$. The main drawback of this structure has been observed to be hysteresis and bistability (see Figure 2.5). In particular, this last characteristic is due to the nonlinear saturation of the quantum dots absorption which is in turn caused by the state filling and the electroabsorption originated by the quantum confined Stark effect.

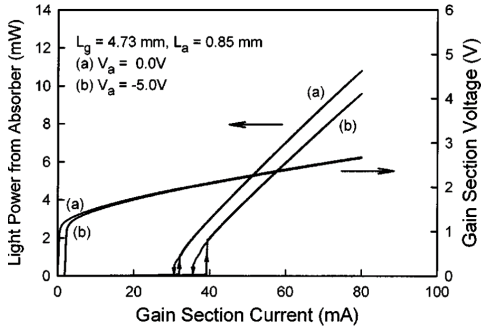

Figure 2.3: Electrical characteristic for different values of reverse voltage of SA. [24]

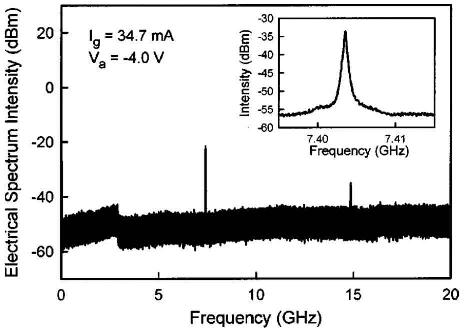

Figure 2.4: Power spectrum at optimal bias conditions. [24]

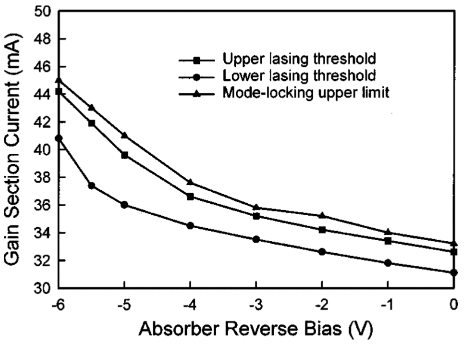

Figure 2.5: Mode-locking and bistability region. [24]

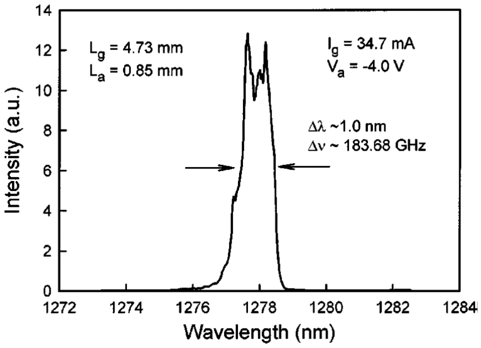

Figure 2.6: Optical spectrum of the laser under optimal bias conditions. [24]

The authors were able, assuming a hyperbolic secant-squared pulse, to establish a repetition rate of 7.4GHz where the narrowest pulse is achieved for a reverse bias of SA between -5.5V and −4 V. The width of the generated pulses is approximately 17 ps.

2.3.2 Recent Outcomes

Since 2018, the research activity about QD-based lasers in the mode-locking regime is growing more and more. The first study in this sense was presented by Lu et al. [45]. Their research involved a InAs/InP quantum dot coherent comb laser (CCL) able to emit in the C-band. The structure, represented in the Figure 2.7, is constituted by an undoped core of five layers of InAs QDs with $In_{0.816}Ga_{0.814}As_{0.392}$ $P_{0.608}$ barriers surrounded by a top p-doped and a bottom n-doped layers of InP. The system is finally capped with a heavily n-doped cap layer (in order to facilitate the fabrication of the ohmic contact), and cleaved to constitute a Fabry-Pérot cavity whose length is about 1225 µm.

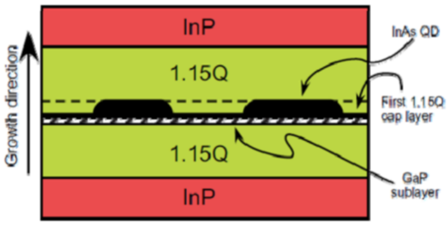

Figure 2.7: Detailed structure of the InAs/InP laser investigated by Liu et al. [45]

The designed system is characterized by an RF beat signal frequency of 34.462 GHz when the system is driven by a current of 390 mA at an operating temperature of 20 °C. In this way a pulse train is achieved in such a way that the pulse width is 800 fs and the center wavelength is 1537.77 nm.

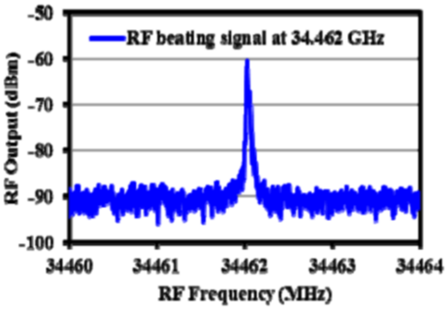

Figure 2.8: Beating frequency of the RF extracted signal. [45]

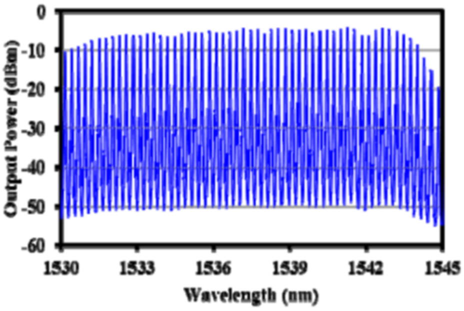

Figure 2.9: Output power spectrum of the CCL module. [45]

The authors also investigated the noise that influences the device, inducing fluctuations of intensity in the time domain. This was done by extrapolating the relative intensity noise (RIN) from a proper measurement system. Lu et al. demonstrated the possibility of achieving RIN values of less than $-165.6\,\mathrm{dB\,Hz^{-1}}$ for such combined combs in the frequency range between 10 MHz and 10 GHz. To realize more industrially captivating structures, silicon substrates were studied, aimed at supporting silicon photonic solutions. Liu et al. demonstrated that a repetition frequency of about 31 GHz is achievable with a single-section QD mode-locking laser directly grown on a (001) GaP/Si substrate [39]. The unique section is driven by a forward bias current at a temperature of 20 °C. They identified a threshold current of 34 mA with a sharp peak in the power spectrum around 30.78 GHz when the bias current is 470 mA. The so-generated pulse has a width of 490 fs.

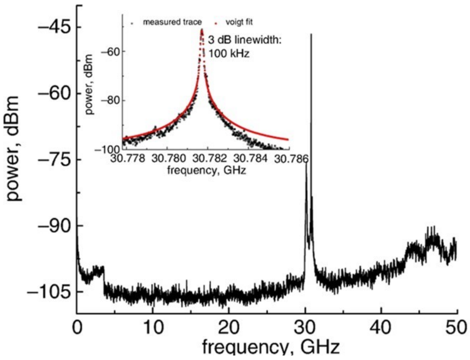

Figure 2.10: RF spectrum of the laser with a zoom aroud 30.78 GHz. [39]

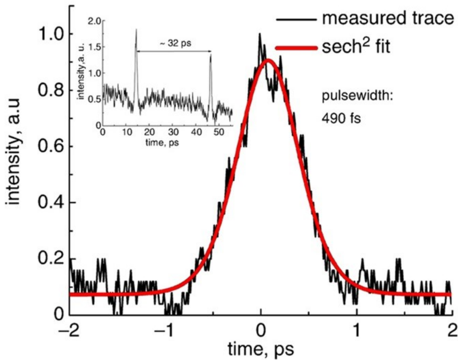

Figure 2.11: Autocorrelation trace of the second harmonic with a $sech^2$ fit [39]

The same research group also investigated more complex structures such as the one in Figure 2.12 where, different from the previous study, they introduced a SA to design a passive mode-locking system [41].

In this case, the QD mode-locking laser was grown on a (001) Si using two layers of GaP and GaAs as buffers. This is done to minimize the effects on laser

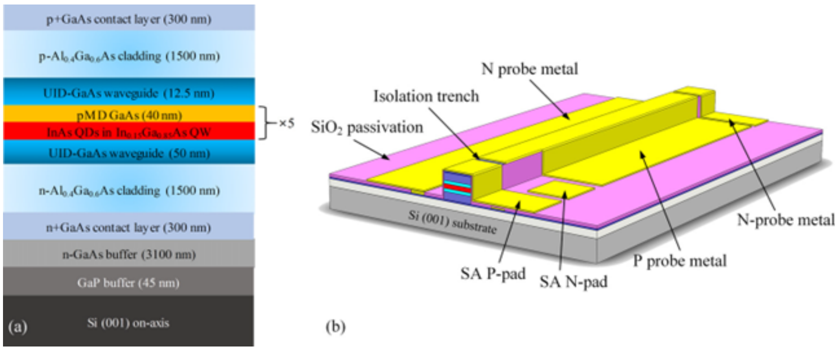

Figure 2.12: Diagram of the InAs quantum dot grown on GaAs/Si substrate with a SA and a gain section [41]

performance of dislocation that may occur in the growing process. In this way, the authors succeeded in realizing a 4500 µm long Fabry-Pérot cavity which is able to impose a repetition frequency of 9 GHz. A performance study was conducted to investigate the dependence of the SA section length ratio with respect to the total length. The ratios of 3%, 8%, 13% and 23% were analyzed by observing a hysteresis effect on power behavior.

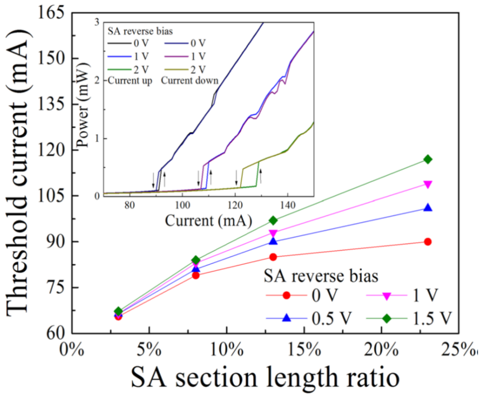

Figure 2.13: Threshold currents trends as a function of the SA length ratio with respect to total length. Inset shows the hysteresis behavior of the power in the case of a 23% ratio. [41]

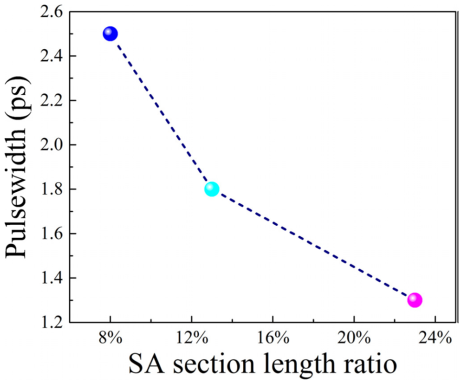

Figure 2.14: Autocorrelation trace of the second harmonic with a $sech^2$ fit [41]

Regarding the threshold current, it is increasing as the length of the SA increases but what is most interesting is the fact that applying different voltages to the SA it varies lesser for low ratio structures with respect to the ones at higher ratio. This happens because, for short SAs, the quantum-confined Stark effect is lower. Finally, Liu et al. found that the different SA length ration impacts also on the width of the pulses which decreases as the length of the SA increases. Furthermore, a larger reverse bias voltage implies a narrower pulsewidth. The aforementioned device was improved by the authors in 2019 using a chirped QD design to broaden the FWHM of the gain spectrum and varying the InGaAs layers width from 3 nm to 7 nm. [40] The result is a device more suited for transmission operation, operating in O band and able of a transmission capacity of 4.1 terabits per second. This was achieved designing a FP cavity of 2048 µm long in which the ratio between SA length and gain section's one is 14%. A passive mode-locking regime is, therefore, established varying the forward current from 75 mA to 200 mA and the reverse voltage from −5 V to −1 V. In this way, pulses whose length is less than 12 ps are achieved, the narrowest of which is calculated to be 5 ps assuming the shape of the hyperbolic secant squared pulse. The paper also observes the possibility to shorten the pulse width increasing the SA section length. In frequency domain, a sharp power peak is seen at 20.02 GHz with a SNR of 64 dB. It is noticeable the fact that the fundamental RF peak SNR is larger than 50 dB (Figure 2.17), hence, a good quality mode-locking regime in the full spectral range is established.

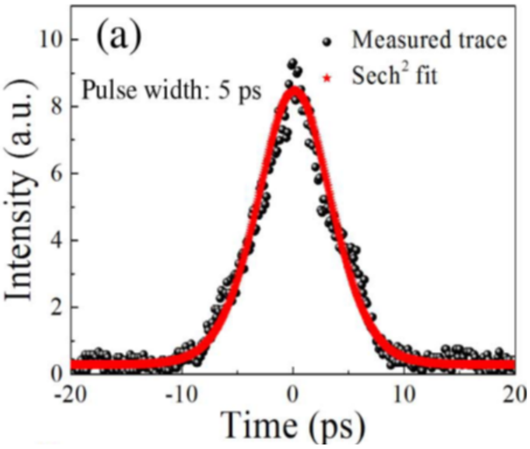

Figure 2.15: Autocorrelation trace of the 20 GHz mode-locking QD based laser with a hyperbolic secant square pulse fitting. [40]

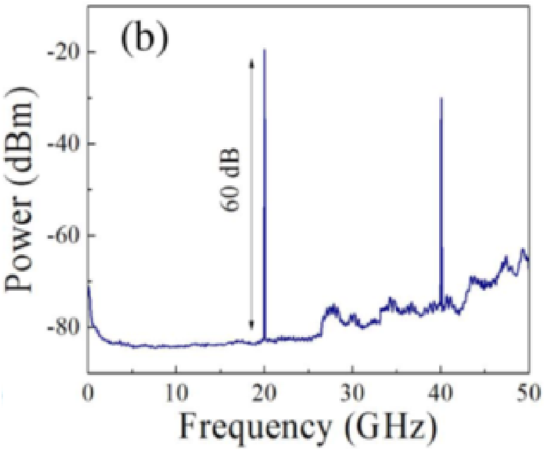

Figure 2.16: RF spectrum of the 20 GHz mode-locking QD based laser [40]

The repetition frequency was slightly further improved by Pan et al. in 2020 reaching a value of 25.5 GHz [47]. In this paper, the authors investigated the behavior of a QD-based two-section frequency comb working in the mode locking regime relying on a structure similar to those of [40] and [41]. They succeeded in demonstrating the existence of stable mode-locking regime over a temperature range between 20° and 120°. This was possible by increasing the number of QD layers, the dot area density and the dot density itself (reaching $5.9 \cdot 10^{10}$ cm^{-2}). To achieve the aforementioned repetition frequency, a cavity of 1615 µm was developed with a gain-to-absorber length ratio of 7 : 1. Pan et al. reported a stable mode-locking results over a wide drive current range from 30 mA to 115 mA and reverse bias voltages −7 V to −1.5 V

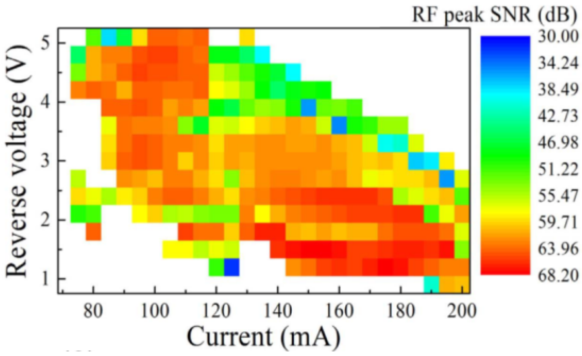

Figure 2.17: Map of RF peak SNR as a function of the bias current and voltage. [40]

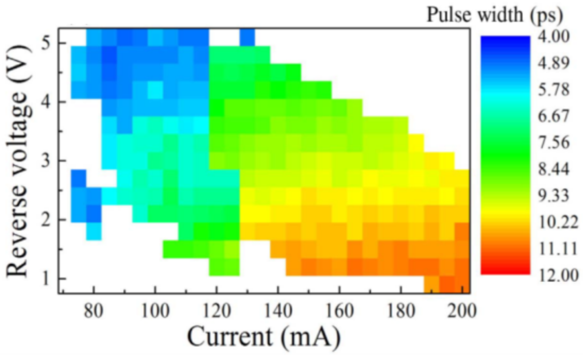

Figure 2.18: Pulse width map as a function of the bias current and voltage. [40]

with the narrowest pulse width of 2.23 ps obtained for (40 mA, −3.5 V). In particular, they noticed how the pulse width increases with the drive current, and it is expected to shorten as the gain-to-absorption ratio decreases. Regarding the temperature behavior mentioned, it is well resumed in Figure 2.24.

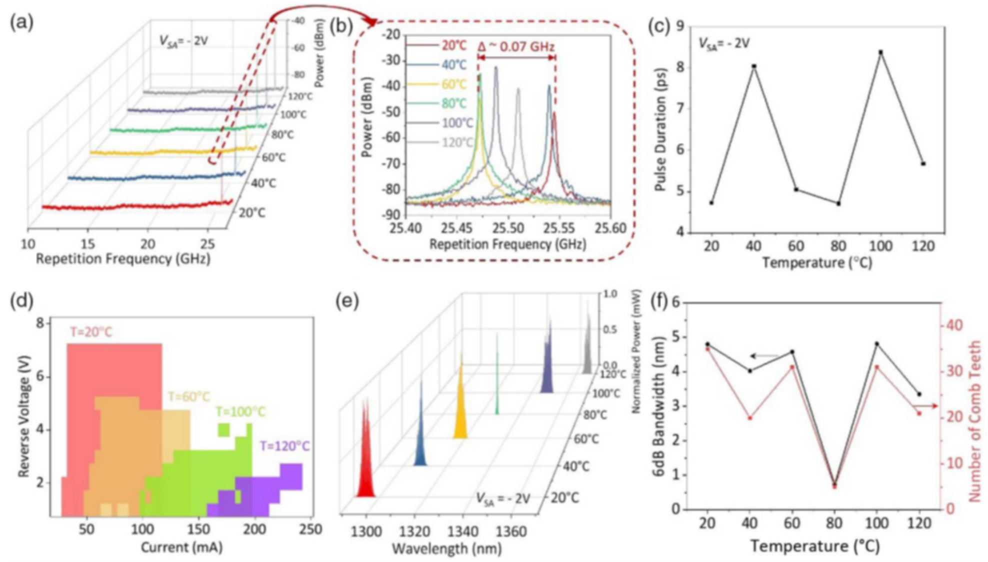

Figure 2.19: a) RF spectrum of two section QD based mode-locking lase with $V_{SA} = -2V$ and $I_{gain} = 49\,\text{mA}, 60\,\text{mA}, 64.7\,\text{mA}, 85\,\text{mA}, 148.5\,\text{mA}, 210\,\text{mA}$, at 20°, 40°, 60°, 80°, 100°, 120° b) zoom of the RF spectrum c) Pulse duration as a function of the temperature d)I-V couples which sustain fundamental mode-locking from 20° to 120° with a SNR> 25 dB e)Optical spectra of the QD mode-locking laser f) 6 dB bandwidth and number of combs teeth involved as a function of temperature [47]

From their simulations, Pan et al. concluded that a stable mode-locking condition could be found over a wide temperature range by adjusting the electrical bias condition even if the achievable mode-locking range is reduced when the temperature increases (Figure 2.24 (d)). On the other hand, high temperatures may induce lasing of the first exited level as a result of the small energy separation between this level and the ground state. Even if in their work the only lasing energy level is the ground state, the absolute mode-locking wavelength shifts as the temperature increases (Figure 2.24 (e)) at a rage which is approximately 0.7 nm/°C. Finally, in Figure 2.24 (f) the 6 dB bandwidth of the device is described. It can be found that a part remains almost constant due to a very narrow comb bandwidth at 80 °C. This phenomenon is not yet fully understood.

In 2021 Wang et al. introduced for the first time a self-injection feedback in a mode-locking laser, monolithically grown on a Si (001). This was done to narrow the RF linewidth to values suitable for coherent communications. They verified its reduction of two orders of magnitude, from 900 kHz to 8 kHz. Their study is reported in [67], where the authors present a comparison between two devices with a single section, with and without the aforementioned feedback. In this paper, they define the strength of the feedback as the optical power ratio between laser output power and the power reflected back into the cavity after one round trip. The feedback strength at which the aforementioned reduction in RF linewidth occurs is −24 dB.

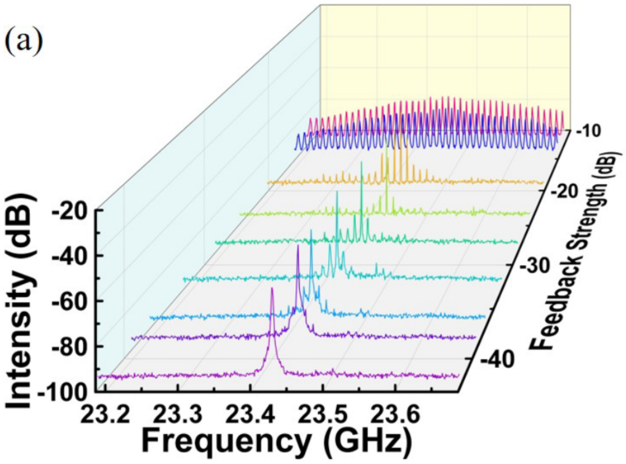

Figure 2.20: RF linewidth variation as feedback strength changes from −12 dB to −45 dB. [67]

As can be clearly seen in Figure 2.20, three main regimes are defined as the feedback strength decreases. In fact, as it weakens and weakens, the line width of the RF signal is rapidly reduced, and the narrowest beat signal occurs when the feedback strength is −24 dB. The coherence collapses with a feedback strength of −15 dB. Investigating this structure is investigating in free-running conditions, Wang et al. demonstrated a stable mode-locking beat signal of 23.45 GHz when a current of 195 mA is injected into the gain section. Particularly relevant in this sense are

Figures 2.21 and 2.22 which analysis how the optical and RF spectrum changes when the injected current varies from 100 mA to 210 mA.

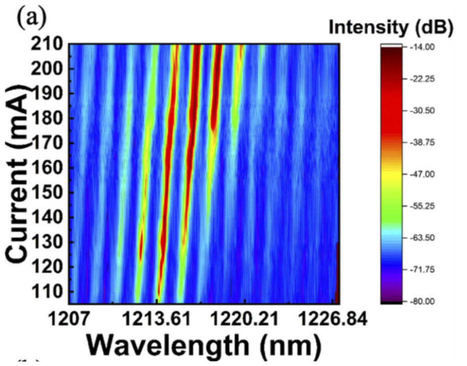

Figure 2.21: Optical spectrum evolution from 100 mA to 210 mA [67]

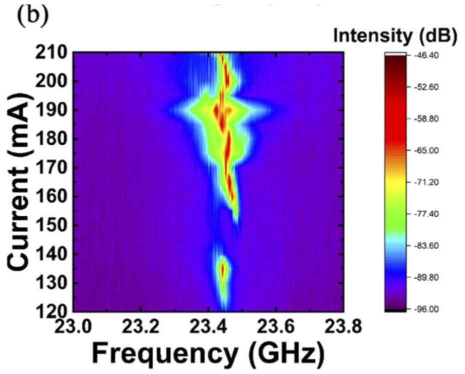

Figure 2.22: RF spectrum evolution from 100 mA to 210 mA [67]

Akahane et al. made a significant improvement from a repetition frequency point of view [1]. They noted that there is a limit in the possibility of stacking QD-layers because of the accumulation of strain. To overcome this problem, it is necessary to adopt strain compensation techniques at the level of the substrate, which enables stacking of more than 100 layers of QDs without compromising the crystal quality and avoiding degradation phenomena. To this aim, they used a n-type InP(311)B substrate that allows round-shaped InAs QD to grow on its surface. In this way, they realized a two-section QD-based mode-locking laser and analyzed how the bias voltage applied to SA the impacts on the optical performances. In particular, the −2 V, 0 V and 2 V bias conditions were analyzed leading to different spectrum and threshold behavior (Figure 2.23).

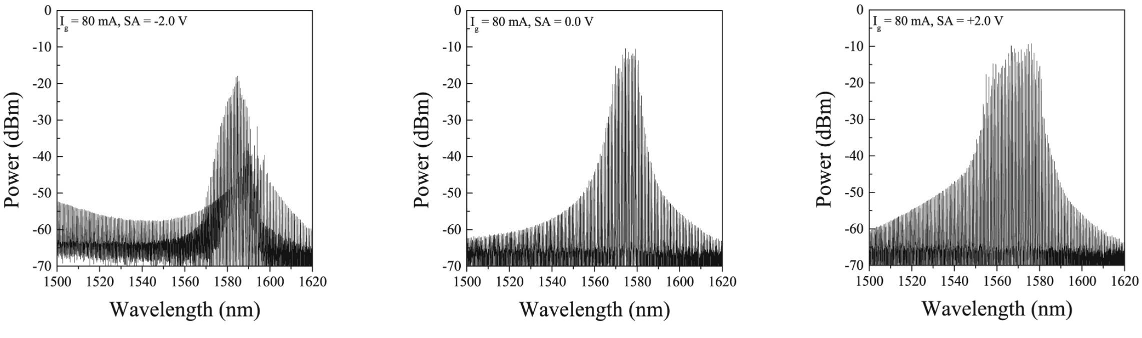

(a) (b) (c)

Figure 2.23: RF spectrum of laser developped by Akahane et al. [1] in $-2, 0, 2V$ - $80mA$ condition.

What is more interesting is to notice the separation of the longitudinal mode in the zoom shown in the Figure 2.24. The authors observed that this value is

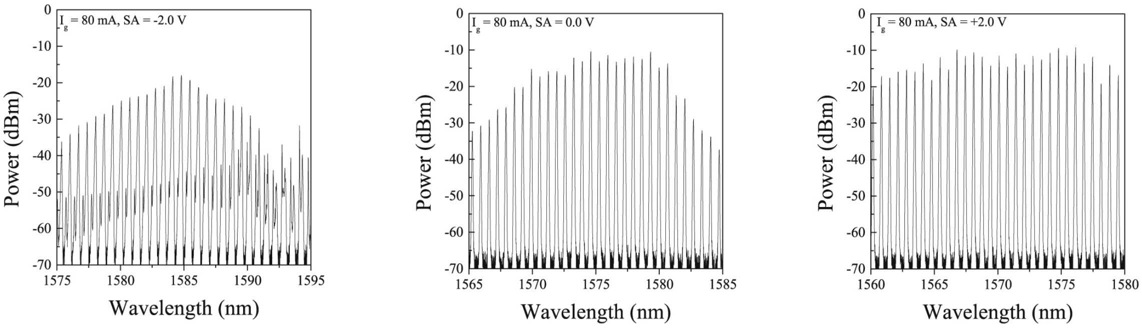

(a) (b) (c)

Figure 2.24: RF linewidth variation as feedback strength changes from $-12\,\mathrm{dB}$ to $-45\,\mathrm{dB}$. [1]

approximately $0.668nm$, which corresponds to a frequency of 81.1 GHz, a value that is consistent with that expected from the calculation of the repetition frequency of the length of the FP cavity. Under these conditions, the pulse width is reported to be 1.85 ps, 853 fs, 464 fs. Instead, the evaluated bandwidths are, respectively, 4.54 nm, 8.34 nm, 15.11 nm. A more complete picture in this sense is given in the Figure 2.25 in which the increase in the spectrum bandwidth is observed with the injected current and the applied bias. The authors also observed that their results seem in contrast with the literature written so far , since, normally, a larger negative bias induces a small pulse width in the time domain (with an increase of the spectrum bandwidth). They explained this discrepancy considering the extremely high QD density of this device inducing a large absorption, which, in contrast, causes a reduction of the gain band width. As a result, a positive bias applied to the SA region optimizes the generation of short pulses.

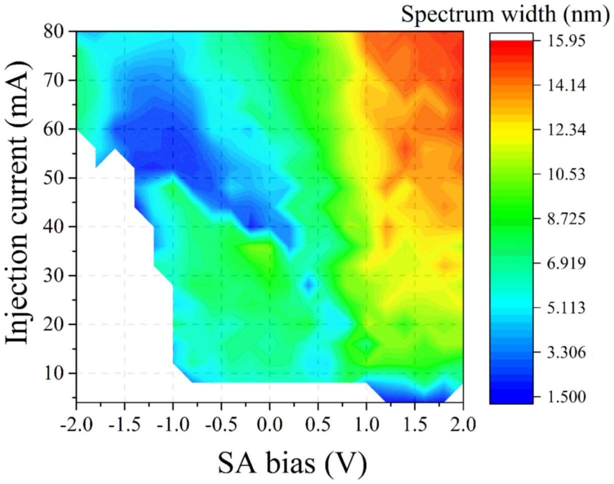

Figure 2.25: RF spectrum of laser developped by Akahane et al. [1] in $-2, 0, 2V$ - $80mA$ condition.

In addition, they assisted to the rise of a high phase noise when the SA is biased with a reverse voltage. Also, other mode-locking regimes are possible. As an example, it is possible to report on the work of Dumont et al. [14]. They designed a QD mode-locking laser operating in harmonic mode-locking condition to transmit in O-band. The key for the achievement of such a purpose is the design of a 5 layers quantum dots in a well structure consisting of 2.5 monolayers of InAs in a 7 nm thick $In_{0.15}Ga_{0.85}As$ well. In addition, layers of 37.5 nm of GaAs were used as separation. This structure was used to work as a comb source for DWDM applications, and it can operate with a repetition frequency of 60 GHz. They proposed results for three basic configurations in which the SA ratio with respect to the total length of the cavity (2048 µm) is 6%, 10%, 18%. A comparison of the third harmonic of the aforementioned laser is described in Figure 2.26 where the label ”foward bias” refers to the situation in which the SAs are connected in parallel to the gain section, and instead the label ”2 V” refers to the situation in which the SAs are driven by a -2 V voltage.

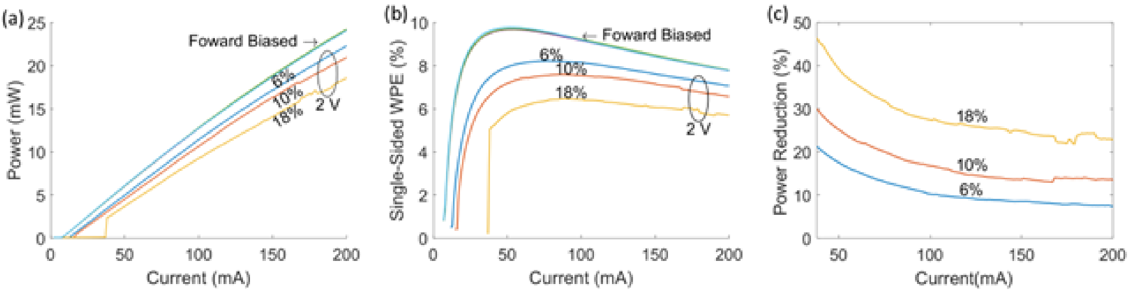

Figure 2.26: Trends of a) optical power b) single-sided wall plug efficency c) the percent reduction in power with respect to forward-biased power. [14]

The results revealed expected behavior, the reduction of the output power as the reverse bias applied in SAs increases in modulus. Moreover, in the forward-biased system, it is possible to assist in performances similar to those of a FP cavity without SAs. Regarding bandwidth, the authors considered to remove states with less than 15 dB SMSR (Side Mode Suppression Ratio). Under this condition, 10% is demonstrated to be the configuration in which the largest 6 dB bandwidth is achieved. In particular, the number of comb lines in the state with the largest $6dB$ bandwidth for 6%, 10%, 18% are respectively 30, 42, 35. The authors also analyzed the power of the lowest line (PoLL) for all the aforementioned configurations in the case of a continuous 20-line comb. They found that the 10% configuration is the one with the the highest PoLL value of -5.1 dB m if compared to the -6.1 dB m of 6% and the -5.2 dB m of the 18%. Another point of care is the lifetime analysis of QD-based mode loking lasers. This aspect was analyzed by Qin et al. in a very recent paper [50]. The structure is composed of three identical SAs of 50 µm and four gain sections that make up a cavity whose total length is 1580 µm (measure that also comprehends the length $10\mu m$ of the isolation layers between one SA and a gain section). In such a structure, measurements of high-temperature reliability of a InAs QD-based laser working in the harmonic mode-locking regime are exploited. To this end, a preliminary threshold current analysis was performed at an operating temperature of $80°C$ beginning to collect results at 336 hours from the beginning of the experiment and ending at 1728 hours. The main results in this sense are reported in Figures 2.27 and 2.28. As can be seen, at the beginning of the experiment, the threshold current is 69.6 mA and after 1392 hours it is 72.74 mA with a percent change of 4.5%. Instead, the output power is reduced by 7%.

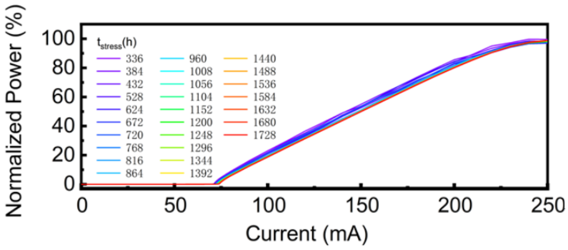

Figure 2.27: Optical power as a function of the injected current [50]

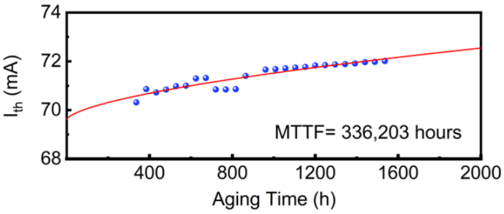

Figure 2.28: Threshold Current as a function of time [50]

The authors reported an exponential fit of the aforementioned data in order to compute the laser failure, a parameter defined as the increase in the threshold current by 1% [56, 58, 68]. The fitting is reported to be the following:

$$I_{th} = I_{th}(0)(1 + at^m) \tag{2.6}$$

where a and m are constants to be determined by fitting and t is the time. In this way, the mean time to failure can be determined as:

$$MTTF = \left(\frac{1}{a}\right)^{\frac{1}{m}} \tag{2.7}$$

parameter that turn to be nearly 38 years, indicating a long lifetime on stress conditions 80 °C. Also, the wavelength stability was investigated. In particular, the analysis was carried out at three different temperatures: 23 °C, 55 °C, 80 °C (Figure 2.29). From the Figure 2.29 it is clear how the wavelength remains stable for a long time, even if the wavelength may drift by an integer multiple of the fundamental frequency (in this case $n \cdot 25$ GHz) due to the competitions of the locked modes.

Long-term stability is not the only feature of this device. Indeed, the aforementioned stability coupled with the 100 GHz repetition frequency makes it a possible candidate for a multi-wavelength laser source in telecommunication applications. As a final remark, we report the results elaborated by Liu et al. on the comparison between the performances in telecommunications field of Quantum Dots and Quantum

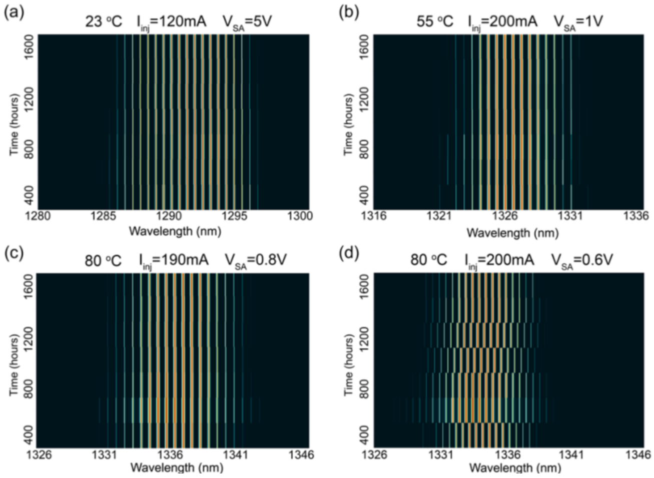

Figure 2.29: Temporal analysis of wavelength stability performed in different bias conditions in 1400 hours. [50]

Dashes for the transmission in C-band of a mode-locking laser made by InAs/InP [37]. The last quantum objects exhibit an improved repetition frequency stability and a lower threshold current loss. In particular the repetition frequency of such a device in the case of Quantum dots and Quantum Dash are respectively 28.36 GHz and 28.42 GHz. Quantum dashes could be the future substitute for Quantum Dots.

2.3.3 Final Considerations

As demonstrated in the previous paragraph, the solutions that can take advantage of QDs for the generation of a train of pulses are various, which makes them a feasible feature for use in telecommunications. For this reason, the literature on this topic is abundant, and it would be impossible to illustrate the complete state of the art. On the other hand, the solutions presented can be summarized in the following table 2.1 to constitute a useful tool to compare each study. In its realization, the layout proposed by Groppo in [18] was adopted. For the sake of completeness, also studies written before 2018 are reported.

2.4 MS-DDE Model

In performing our simulation, it is necessary to establish a model which calculates the optical and electronic parameters needed to fully understand the physical and electrical behavior of the simulated laser. Several techniques could be used, but, in any case, the basis above which all the models must be constructed is the so-called

Ref.	Year	ML type	$\lambda (\mu m)$	f_R (GHz)	$\Delta\tau$	P_{max} (mW)
[24]	2001	P	1.3	7.4	17	-
[60]	2003	P,H	1.1	10	<14	4
[62]	2004	P	1.3	18	10	2.5
[51]	2005	P	1.3	21	<2	1100
[70]	2005	P	1.3	5.2	5.7	290
[21]	2005	P	1.3	5	$3.2 \div 7$	<1700
[61]	2005	C	1.1	10×2	7	-
[6]	2006	P,H	1.3	$20 \div 80$	$0.5 \div 2$	-
[32]	2007	P,H	1.3	40	2	-
[38]	2008	S	1.5	92.5	<1	-
[43]	2008	S	1.5	45	0.312	-
[44]	2009	S	1.5	46	0.445	-
[59]	2009	P	1.3	20	1	105
[35]	2009	P	1.2	10	10	-
[36]	2010	P	1.3	5.1	-	-
[45]	2018	S	1.5	34	29	-
[39]	2018	P	1.3	31	0.49	40
[41]	2018	P	1.3	< 9	1.3	-
[40]	2019	P	1.3	20	<12	-
[47]	2020	P	1.3	25.5	<9	-
[67]	2021	P	1.5	23.5	-	-
[1]	2021	P	1.3	81	<1.85	-
[14]	2022	C	1.3	60	-	-
[37]	2023	C	1.3	28.36	-	-
[50]	2024	C	1.3	100	-	-

Table 2.1: Summary of the most significant characterising describing the state of the art of QD-based mode-locking lasers. In the third column the mode-locking type is summarized as follows: P (passive mode-locking), H(hybrid mode-locking), S(self mode-locking), C(colliding mode-locking)

traveling wave equation:

$$\pm\frac{\partial V^{\pm}}{\partial z}+\frac{1}{v_g}\frac{\partial V^{\pm}}{\partial t}=-\frac{\alpha_i}{2}V^{\pm}-j\frac{\omega_0}{2c\varepsilon_0 n_{r,0}}\Gamma_{xy}P^{\pm}+F^{\pm} \tag{2.8}$$

where V is the field amplitude in time domain,v_g is the group velocity, α_i is the intrinsic wave-guide losses, P is the polarisation and F is the spontaneous emission noise. The "±" is associated with the description of the forward or backward component of the field. In any case, the traveling wave equation must be solved in accordance with suitable boundary conditions. Among the possible methods, a first example could be a time domain traveling wave (TDTW) model whose main feature is the solution of (2.8) in a finite difference scheme approach. The main drawback of these models concerns not only the time required for accurate results, but also the memory which is necessary to allocate to store the solutions [53]. Another possibility is to use the self-consistent pulse profile model, which is the first method proposed from a historical point of view [46, 23]. It is a lumped element-based model in which the main assumption is the fact that the widths of the pulses are much smaller than the repetition period. Although many studies implement these models, they have limited applicability. The trade-off between accuracy, the requested elaboration time, and the memory that must be allocated is represented by the Delayed Differential Equation Model (DDE). In this thesis, this model is adapted in a multi-section sense (MS-DDE) to obtain the results presented in the next chapter.

2.4.1 Assumption of the MS-DDE model

In the description of our results, we take advantage of the model developed by Rossetti in [52] on the basis of the models described in [64] and [63]. Detailed derivation of the model starting from the Traveling wave equation is beyond the scope of this thesis, but is well explained in [31] and [64]. The main assumption that constitutes the starting points of the model used in our simulations is as follows:

1. The consideration of a unidirectional ring cavity laser.
2. The alternation of gain (G) and saturable absorber (SA) sections.
3. The intrinsic waveguide losses α_i are modeled as a lumped element in $z = 0$ as well as the finite-gain spectral bandwidth which produces a filtering effect.

For the sake of completeness, the model which is actually implemented in our computational analysis is a modified version of the ones reported in the aforementioned literature. Indeed, what is analyzed is not a single combination of one gain section and one SA, but a repetition of this basic structure. As we will demonstrate in the following chapter, the smaller the length of the cavity, L, the higher the repetition rate, f. An example of the considered structure is depicted in Figure 2.30

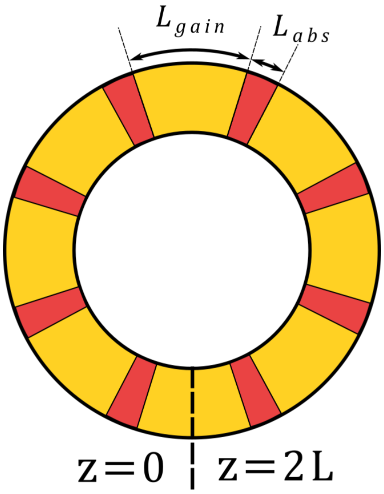

Figure 2.30: Ring structure analysed with the modified multi section model implementing the DDE equations.

in which a device with 8 active regions (yellow) and 8 saturable absorbers (red) is described.

In this frame, each section (made by the gain medium or the saturable absorber) is considered to be isolated from each other and can be biased independently. In addition, a non-saturable loss term is introduced at any interface between different sections.This allows one to better model the intrinsic waveguide losses α_i, allowing one to extract the internal signal at any interface. In order to properly describe the DDE, a change of variable is necessary:

$$t \rightarrow \tau = t - \frac{z}{v_g} \tag{2.9}$$

In general, in this approach, the field at a generic instant τ is related to the field in the instant $\tau + T_R$ by the following differential equation:

$$\frac{dV_i(\tau)}{dt} = -\Gamma V_i(\tau) + \Gamma R_i(\tau - T_R)V_i(\tau - T_R) \tag{2.10}$$

where i is the label which can denote any energy level considered, R is the round trip gain and the term Γ is half of the FWHM of the Lorentzian filter that entails the inhomogeneous broadening.

2.4.2 Mode-locking Condition

In order to fully understand which condition must subsist in order to guarantee the mode-locking regime, a simple reasoning could be done performing a steady state analysis. Indeed, neglecting the temporal derivative in the equation (2.10) it becomes:

$$V_i(\tau) = R_i(\tau - T_R)V_i(\tau - T_R) \tag{2.11}$$

The previous equation is equivalent to say that the field after a period is equal to the field at the beginning of the time reference except for a the round trip gain $R_i(\tau - T_R)$. To achieve stable mode-locking the field must not experience changes during the propagation in the cavity, therefore:

$$V_i(\tau) = V_i(\tau - T_R) \tag{2.12}$$

This condition is verified only when the Round Trip Gain after a period is equal to the the Round trip gain at the time τ. In symbols:

$$R_i(\tau - T_R) = R(\tau) = 1 \tag{2.13}$$

More accurately, the possibility to have instabilities when the ML pulse power is zero must be considered. In fact, when

$$R_i(\tau - T_R) = R(\tau) < 1 \tag{2.14}$$

spontaneous emission noise arise. In short,

$$V_i(\tau) = V_i(\tau - T_R) \Longleftrightarrow \begin{cases} R_i(\tau - T_R) = R(\tau) = 1, \; V_i(\tau) \neq 0 \\ R_i(\tau - T_R) = R(\tau) < 1, \; V_i(\tau) = 0 \end{cases} \tag{2.15}$$

It is noticeable that in this picture we have assumed implicitly that the gain bandwidth is infinite. Indeed, (2.10) could be rewritten as:

$$\frac{1}{\Gamma}\frac{dV_i(\tau)}{dt} = -V_i(\tau) + R_i(\tau - T_R)V_i(\tau - T_R) \tag{2.16}$$

Therefore, the left hand term is zero not only when the derivative is zero but also when $\Gamma \to +\infty$, condition which is equivalent to say that the the gain bandwidth is infinite. In order to perform a complete analysis, a limited bandwidth must be considered. More specifically, a Lorentzian bandwidth limiting element is introduced in the reference $z = 0$ influencing the pulse propagation at every round trip. In this optics, the derivative term cannot be neglected anymore and a filtering effect arises. For these reasons, it is possible to demonstrate that the field at the time τ is rewritten as a convolution product:

$$V_i(\tau) = \Gamma e^{-\Gamma\tau} \circ (R_i(\tau - T_R)V_i(\tau - T_R)) \tag{2.17}$$

where ”$\circ$” denotes the convolution product.

2.4.3 Output and Stimulated Emission Power

In the computational analysis performed, it is fundamental to take into account the carrier evolution in the cavity. To this aim. the entire cavity is divided in slices so that, if it is considered that there are F slices, the total length will be:

$$L = \sum_{k=1}^{F} L_k \tag{2.18}$$

where the k subscript identify the k-th slice. Hence, in the preceding equations the period is:

$$T_R = \frac{1}{v_g} \sum_{k=1}^{F} L_k \tag{2.19}$$

In order to estimate the output and the stimulated emission power, the round trip gain must be must be calculated. This quantity will depend on both non linear gain and absorption dynamics and can be calculated as:

$$R_i(\tau) = \prod_{k=1}^{F} B_{i,k}(\tau) M_k \tag{2.20}$$

where i is the index that indicates the energy level considered, M_k is the non-saturable losses localized at the interface between the section k and $k+1$ and $B_{i,k}(\tau)$ is a coefficient which takes into account the amplification or the attenuation and the phase charge experienced by the field at the interface between one slice and another. In particular,

$$M_k = \sqrt{K_k} e^{-\frac{\alpha_i}{2} L_k} \tag{2.21}$$

Instead, the expression of the coefficient $B_{i,k}$ depends on the energy level considered. Here we report the ones associated to the ground state (GS) and first exited state (ES1) which are the only relevant energy levels in our analysis.

$$B_{GS,k} = e^{\Gamma_{xy} \overline{g}_{GS,k}(\tau) L_k} \cdot e^{j\beta \Gamma_{xy} \overline{g}_{ES1,k}(\tau) L_k} \tag{2.22}$$

$$B_{ES1,k} = e^{\Gamma_{xy} \overline{g}_{ES1,k}(\tau) L_k} \cdot e^{-j\beta \Gamma_{xy} \overline{g}_{GS,k}(\tau) L_k} \tag{2.23}$$

In previous two equations, the coefficient $\overline{g}_{i,k}(\tau)$ is the average gain/absorption in the $k-th$ slice and can be computed as:

$$\overline{g}_{i,k} = g_{0,i}(2\overline{f}_{i,k}(\tau) - 1) \tag{2.24}$$

where $\overline{f}_{i,k}(\tau)$ is the occupation probability of the $i-th$ quantum dot in the k slice and varies in the time according to the rate equations:

$$\frac{d\overline{f}_{i,k}(\tau)}{d\tau} = \overline{R}_{i,k}^{in}(\tau) - \overline{R}_{i,k}^{out}(\tau) - \overline{R}_{i,k}^{st}(\tau) \tag{2.25}$$

where the first two rates are the input and the output ones, and $\overline{R}_{i,k}^{st}$ è the stimulated emission rate which can be calculated, following the same reasoning proposed in [64] as:

$$\overline{R}_{i,k}^{st}(\tau) = (|(B_{i,k}(\tau)|^2 - 1) \left(\prod_{m=1}^{k-1} |B_{i,k}(\tau)|^2 M_m^2 \right) \frac{|V_i(\tau)|^2}{\hbar(\varepsilon_{e,i} - \varepsilon_{h,i}) L_k} \tag{2.26}$$

The complete evaluation of $\overline{R}_{i,k}^{in}(\tau)$ and $\overline{R}_{i,k}^{out}(\tau)$ is beyond the aim of this thesis but can be found in [18]. After a round trip, the output power is :

$$P_i^{out}(\tau) = \frac{1-K_F}{K_F} |V_i(\tau)|^2 \tag{2.27}$$

where K_F is the output coupling factor of the ring laser. Now, the power due to the electron-hole recombination could be easily calculated as:

$$P^{st}_{i,k}(\tau) = \hbar(\varepsilon_{e,i} - \varepsilon_{h,i})\overline{R}^{st}_{i,k}(\tau)L_k \tag{2.28}$$

Of course the conservation of energy must hold, therefore the stimulated power can be also written as:

$$P^{st}_{i,k}(\tau) = \prod_{m=1}^{k} |B_{i,k}(\tau)|^2 M_m^2 |V_i(\tau)|^2 - \prod_{m=1}^{k-1} |B_{i,k}(\tau)|^2 M_m^2 |V_i(\tau)|^2 \tag{2.29}$$

where the first term represents the output power and the second one is the input power. Of course, the conservation of energy holds if there are not present dissipative effects. In this optics, such condition can be assumed if no additional non-saturable losses are distributed in the cavity but only modelled as located at the interface between adjacent sections.

Chapter 3

Simulation Results

The main objective of this thesis is the simulation of a ring-cavity laser using a delayed differential equation model to compute the dynamical evolution of the density of charges and optical quantities. To this aim, a preexisting program improved by Groppo [18] was used. This program has demonstrated high flexibility allowing the user to establish at the beginning both physical and geometrical constraints to be simulated. Our contribution is mainly focused on using such a program to demonstrate that this model predicts the possibility of designing lasers whose operating frequency is in the subterahertz regime (0.1-0.2 THz). Of course, also the stability was taken into account and represents a very restrictive constraint to be fulfilled. The aforementioned program is suitable for the simulation of passive and harmonic mode-locking technique. The main steps which must be followed for the simulation of these kind of devices taking advantage of the MS-DDE model developed by Rossetti [52] and using the algorithm of Groppo [18] are the following:

1. Identification of the physical and geometrical parameters of the laser. Practically, it consists of designing the number of sections which compose the cavity and establishing the optical characteristic constant that will be used in the DDE computation.

2. Identification of the laser bias condition. This basically means identifying which voltages, applied on SA, and current, injected in gain sections, are suited to sustain stable mode-locking at the required frequency. In our simulations the SAs will be subjected to a reverse bias. In the following, we will assume that the injected current is uniform and that the bias of the SAs is not subjected to fluctuations.

3. Simulation and adjustment of the parameters to optimize the results and their performance.

In our work, we have also analyzed the impact of the change of the SA's length with respect to the entire length of the cavity. As we will illustrate, frequencies of 180

GHz are simulated in an 18-section device. The main purpose of this device is the extraction of the RF component from the SA which will be irradiated by means of an properly designed antenna. This is why ring cavities are employed: they are not only more energetically advantageous than a Fabry-Perot one (no power is wasted at the facet) but also geometrically (they have a reduced footprint).

3.1 Multi Section Modelling of Ring Cavities

As done did for a 8-section device [18, 19], the preexisting DDE model is adapted to a multi-section reality. To fully understand what the main features of such modifications are, it is easier to think about the structure depicted in the Figure 3.1. It consists of a cavity of two isolated sections (one gain and one SA section), each of which is subdivided into slices so that the whole cavity is composed of F portions.

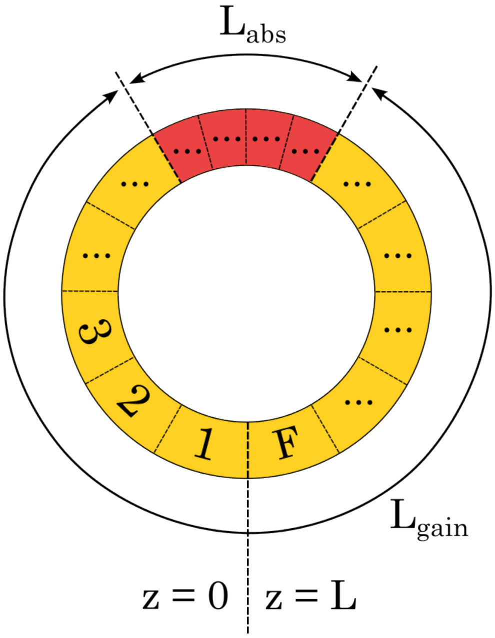

Figure 3.1: Basic two section ring structure in which the length of SA and gain section are labelled as respectively L_{abs} and L_{gain}.

The output signal will be extracted in the F^{th} slice, at the coordinate $z = 0$, that is, in the middle of the first gain section. Since part of the radiation must be extracted, the F^{th} slice must have a different power transmission coefficient with respect to the other. We assumed that such a parameter is:

$$K_k = \begin{cases} 1, & k = 1, 2, ..., F-1 \\ 0.9, & k = F \end{cases} \tag{3.1}$$

This means that the radiation is transmitted without losses inside the cavity, but, after a round trip, the 10% of it is extracted. Of course this choice is arbitrary, in principle the signal can be extracted at any interface between adjacent slices. Therefore, the field after the beginning of the second round trip would be:

$$V_i(t,0) = \sqrt{K_F} V_i(t,L) \tag{3.2}$$

where L is the total length of the cavity and i is the index which can generically indicate the Ground State (GS) or the First Exited State (ES1). Other energetic levels are not considered in our dissertation. Actually, equation (3.2) describes any field after a generic round trip, so it can be regarded as the boundary condition of the wave equation written in the previous chapter. Regarding the round-trip gain, in the previous chapter, we have seen that it can be written as:

$$R_i(\tau) = \prod_{k=1}^{F} B_{i,k}(\tau) M_k \tag{3.3}$$

However a more effective way to implement such parameter is rewrite the previous equation as:

$$|R_i(\tau)| = e^{(G_i(\tau)-A_i(\tau))L} \tag{3.4}$$

where $G_i(\tau)$ and $A_i(\tau)$ are respectively the amplification in a section at the time τ, and the overall saturable and non-saturable losses experienced by the travelling pulses. They can be evaluated as follows:

$$G_i(\tau) = \frac{1}{L} \sum_{k \in G} \ln |B_{i,k}(\tau)| \tag{3.5}$$

and

$$A_i(\tau) = \frac{\alpha_{in}}{2} + \frac{1}{L} \left[\sum_{k \in G} \ln |B_{i,k}(\tau)| + \sum_{k=1}^{F} \ln \frac{1}{\sqrt{K_k}} \right] \tag{3.6}$$

In (3.5) and (3.6), G is the ensemble of all the active regions; similarly, SA will indicate the ensemble of the reversely biased regions. Another feature that must be taken into account is the instability. In particular, after the passage of the pulse in an SA, there is a ultra-fast recovery of the ground state population, which increases the term $G_i(\tau)$ in (3.4). Indeed, such an equation establishes that there would be a net gain for GS when

$$R_{GS}(\tau) > 1 \Rightarrow G_{GS}(\tau) > A_{GS}(\tau) \tag{3.7}$$

inequality which is verified for a certain range of value. In this window, the presence of spontaneous emission noise may cause a trailing-edge instability of the pulses, which is an unwanted effect. The instability is usually much more relevant for the value of the bias current just above the threshold.

3.2 Physical Structure

The model developed so far was first published by Rossetti et al. in [53] and was initially imagined to predict the optoelectronic behavior of an edge-emitting FP cavity-based model depicted in the Figure 3.2.

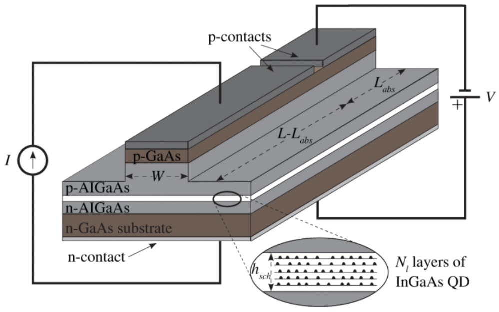

Figure 3.2: Edge emitting passive mode-locking laser based on a FP cavity analysed by Rossetti in [53].

The device is composed by a ridge-waveguide grown on an n-doped GaAs substrate. As Groppo [18, 19], even in our study the only change in this structure is the kind of cavity. Indeed, the shown device is rearranged in order to form the ring cavity depicted in Figure 3.1. The quantum dots are grown in a layer of AlGaAs whose width is labeled h_{sch} realizing a structure named dots in a well whose diagram of the conduction band is depicted in Figure 3.3.

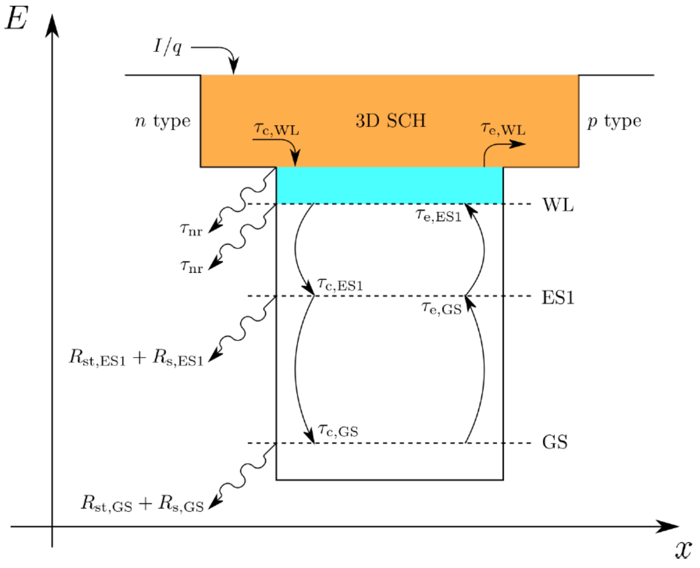

Figure 3.3: Representation of the system considered in this thesis. [19]

This name is due to the fact that discredited energy levels of quantum dots are arranged below a more energetic 2D and 3D structure. Indeed, there is a transition from 3D bulk states (Separate Confined Heterostructure) to the 0D quantum dot states passing through 2D quantum well states of a layer named Wetting Layer. In such a structure, a forward bias provided by the flowing of a current causes the injection of high energetic carriers, which decay, after a certain capture time, at the levels of the quantum dots. Under the application of a reverse bias (such as the one applied to SAs), the carriers are extracted with a characteristic time τ^e called escape time. The exact dynamical analysis of this quantum object is beyond the scope of this thesis, but it is deeply treated in [11] and [18]. However, the exact definition of its geometrical parameters is fundamental for the solution of the MS-DDE model and in the simulation of the ring cavity laser. The main parameter assumed are resumed in the table.

Symbol	Description	Value
d	Ridge waveguide width	6 µm
α_{in}	Intrinsic wave-guide losses	$1.5\,\mathrm{cm}^{-1}$
Γ_{y}	Transversal confinement factor	75 %
Γ_{x}	Vertical confinement factor	10 %
n_{r}	Refractive index	3.66
η_{i}	Internal Quantum Efficiency	85 %
h_{SCH}	SCH height	180 nm
h_{QW}	QW height	7 nm
h_{QD}	QD height	5 nm
N_1	Number of QD layers	12
N_D	QD surface density	$2.85 \times 10^{10}\,\mathrm{cm}^2$
R_{QD}	QD radius	15.5 nm
ΔE^{inh}	FWHM inhomogeneous broadening	34 meV
$E_{(e-h),\mathrm{GS}}$	GS interband transition energy	0.9901 eV
$E_{(e-h),\mathrm{ES1}}$	ES1 interband transition energy	1.0597 eV
$\tau_{\mathrm{c,GS}}$	GS capture time	0.2 ps
$\tau_{\mathrm{c,ES1}}$	ES1 capture time	0.2 ps
V_{bi}	Built-in potential	0.8 V
K_{F}	Power transmission coefficient	90 %

Table 3.1: The principle parameters used in our simulations, the most of which are obtained from .

We also assumed one more characteristic: the unidirectionality of the ring cavity in which the harmonic mode-locking regime is established. Indeed, the bidirectionality of the cavity is a direct consequence of the rotational symmetry. Even if it is not directly implemented in the code, from a technological point of view this characteristic can be promoted by breaking such symmetry. One possibility is to introduce an S-shaped waveguide inside the ring so that a unbalance loss mechanism rises coupled with a non-reciprocal gain between the clockwise and anti-clockwise directions [16]. An example of device operating in this sense is the one depicted in Figure 3.4.

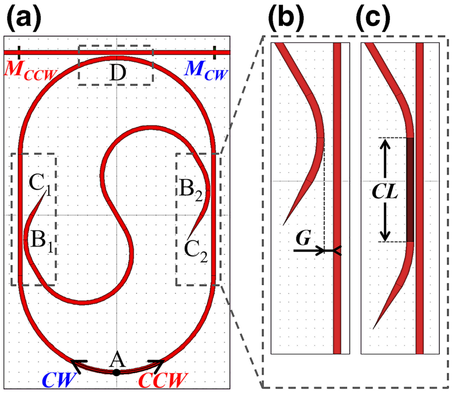

Figure 3.4: Representation of an S-shape waveguide embedded in a ring structure to improve the unidirectionality of the ring WG. A wave is thought to start at a point A in a CW (clockwise) direction and in a CCW (counterclockwise) direction. [16]

In such a configuration, in order to understand the operation of this structure, it could be assumed that a wave starts to propagate in point A in both the CW (clockwise) and CCW (counterclockwise) directions. When it comes near the S-shaped waveguide (in the point B_1) an evanescent coupling is established between the two WGs so that part of the CW signal continues to circulate in the ring, part follows a clockwise path in the S-shaped one. On the other hand, when the CCW signal reaches the point B_2, the same coupling force induces part of the signal to abandon the ring structure, travel through the S-shaped WG, and be reinserted in the ring. In this way, a CCW is induced to restart is flowing in the ring WG with a CW direction. Another possible approach was presented by Kazakov et al. in [28]. It consists of taking advantage of the opticaal properties of the defects which can be introduced in the cavity. Indeed, in proximity, reflection phenomena may increase, affecting the propagation of the pulses. By engeneering them one direction can be tailored to be the most favorable inducing a unique propagation way.

3.3 Simulation of device with 16 sections

Our simulation work began with the design of a device with a repetition frequency of $f = 165\,\text{GHz}$. As stated before, the first step that must be followed is the identification of the physical and geometrical conditions which characterize the device. In order to reach such high frequency, it was doubled the sections he designed, working with a 16 sections device composed by the alternation of gain and SA sections. Their dimensions are computed starting with the desired repetition frequency. Indeed, the repetition frequency will be computed as the fundamental frequency f_R multiplied by the total number of sections divided by 2. Therefore:

$$f_R = \frac{f}{8} = 20.625\,\text{GHz} \tag{3.8}$$

This quantity can be related to the length of the cavity recalling the definition of the fundamental frequency, i.e. the reciprocal of the fundamental period. On the contrary, this last variable can regarded as a ratio between the group velocity and the total length of the cavity, therefore:

$$f_R = \frac{f}{8} = \frac{v_g}{L} = \frac{c}{n_r L} \tag{3.9}$$

where c is the velocity of light in the vacuum equals to $2.998\,\mu\text{m/ns}$ and n_r is the effective refractive index associated to the material. Now, the total length of the cavity can be easily computed as:

$$L = \frac{8c}{n_r f} = 3974.17\,\mu\text{m} \tag{3.10}$$

Assuming that each pair of gain and SA sections are divided in a equal number of slices it can be stated that the length of gain plus SA section is:

$$L_\text{gain} + L_\text{abs} = \frac{L}{8} = 496.77\,\mu\text{m} \tag{3.11}$$

At this point, we made the assumption that the total length of the absorbing sections would be 23.84% of the total cavity. Hence, we imposed that:

$$L_\text{gain} = 378.3\,\mu\text{m} \qquad\qquad L_\text{abs} = 118.4\,\mu\text{m} \tag{3.12}$$

Regarding the number of total simulated slices, the more sections we have, the more accurate the simulations. However, this is paid in terms of computational time, establishing a trade-off between accuracy and time. For this reason, the total number of slices is assumed to be 80, 8 for each gain section, and 2 for each SA. As a final remark, the fact that the formula (3.9) could be generalized including the generic number of the total sections (N_S):

$$f = \frac{N_\text{S}\; c}{2 n_r L} \tag{3.13}$$

It is clear now that the frequency and the total length of the cavity are inversely proportional, implying that to work at a higher frequency, a shorted cavity is needed. This behavior must meet the technological limits to be physically realized. The trend of f as a function of L taking into account the possibility of increasing the number of sections is shown in Figure 3.5.

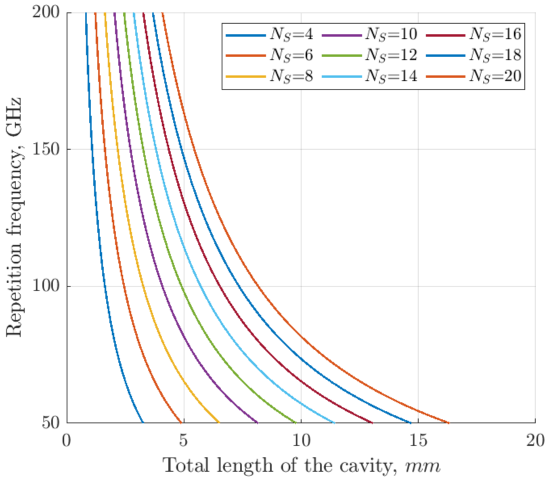

Figure 3.5: Trends of the repetition rate frequency as a function of the total length cavity for devices with different number of total sections.

As is obvious, a chosen working frequency could be reached with different devices made of a different number of sections, changing the total length of the cavity. Returning to the simulation results, the sketch of the simulated cavity is represented in the Figure 3.6. In the following we will illustrate the main figures of merit of such simulations each of which was simulated in the bias window:

$$\begin{cases} I = (175 \div 900)mA & z \in G \\ V = (-6.5 \div -4)V & z \in SA \end{cases} \tag{3.14}$$

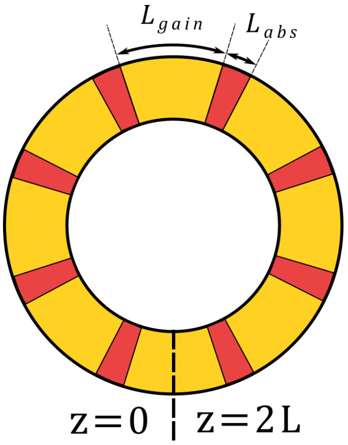

Figure 3.6: the simulated 16-section ring structure.

3.3.1 Repetition rate and stability

The simulation is constituted by the MS-DDE solution for every couple of voltages and currents written in (3.14). The first significant analysis which can be conducted is which couple (V-I) sustains the presence in the cavity of eight pulses in the time regime. In other words, these are the bias conditions for which the ratio between the repetition frequency and the fundamental one is equal to eight.

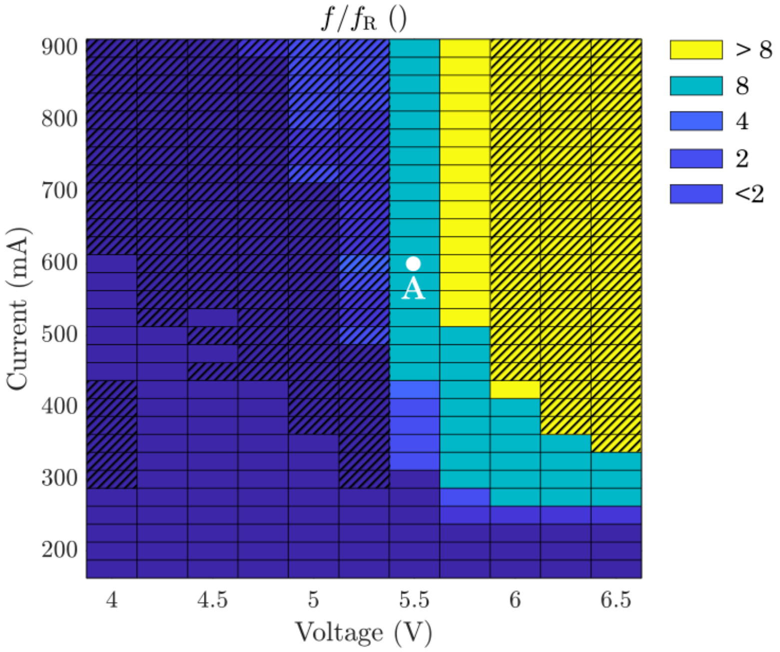

Figure 3.7: Map of the ratio between the repetition rate and the fundamental frequency. The instabilities regions are highlighted with oblique lines.

Another characteristic which must be considered in the analysis of these QD-based lasers is the stability of the ML regime. In our case, we take advantage of Haus's criterion [23] to consider stable the signals whose net gain becomes immediately negative after the passage of the pulse. When this criterion is not verified, the spontaneous emission noise could be amplified, an effect that must be avoided. In the reported Figure 3.7 the regions of instability were dashed out, individuating a region in which a steady state could be reached. Outside this, there are net gain windows that may be amply the spontaneous emission nose. As an example, we report in the time domain the representation of pulses in point A. For the sake of simplicity the representation was limited to a fundamental period which is equivalent to:

$$T_R = \frac{1}{f_R} = 48.48\,\mathrm{ns} \tag{3.15}$$

Figure 3.8 shows pulses with a bit of distortion; however, such condition is not high enough to compromise the reach of a steady state. Instead, representing the

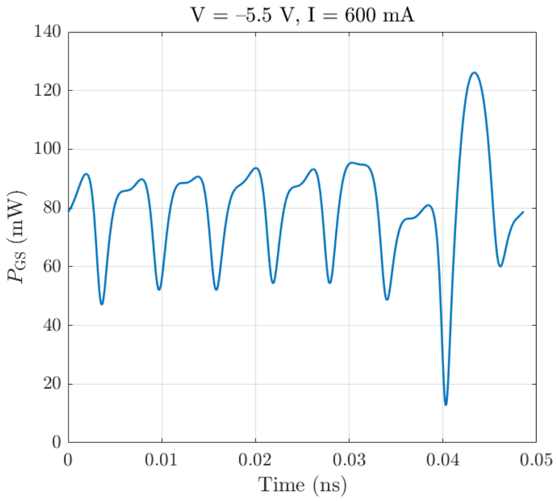

Figure 3.8: 8 pulses in time domain when in the gain section it is injected a current of 600mA and the saturable absorbers are biased with a voltage of -5.5V.

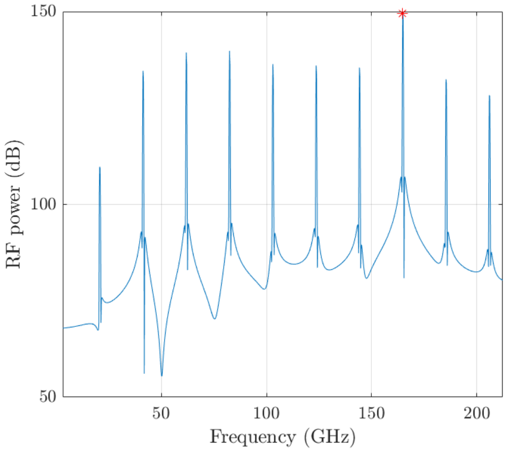

Figure 3.9: RF spectrum of the signal when in the gain section it is injected a current of 600mA and the saturable absorbers are biased with a voltage of -5.5V.

pulses in the frequency domain (Figure 3.9), we will aspect a series of pulses in correspondence to the harmonics which are able to resonate in the cavity. As can be seen, the repetition rate of the cavity corresponds to the main peak in the RF spectrum, which will be therefore a figure of merit to characterize the cavity. Actually, for ideal pulses, the output signals would be sinusoidal, but the presence of higher harmonic spectral lines does not allow us to see such a picture.

3.3.2 Photocurrent and Output Power

Since our simulations are intended to be used in the early stage of designing devices that emit in the RF spectrum, the extracted signal has particular relevance. In fact, for the telecom application, a structure like the one depicted in Figure 3.10 could be realized.

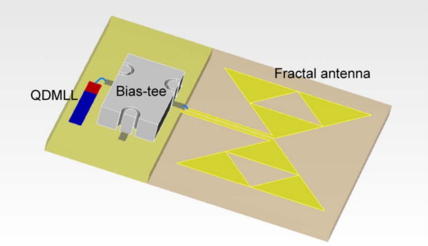

Figure 3.10: Modulus of a RF integrated RF signal generator which may integrate a QD-MLL. [35]

In such a device, the quantum dot based mode-locking laser is integrated with a coplanar waveguide and a bias tee, in a modulus whose main feature is exploited by a fractal antenna for the emission of signals. Therefore, the aforementioned modulus can be considered an RF signal generator and could constitute the basic unit of a more complex array [35]. Regarding our laser, the quantity extracted from the cavity is actually the photocurrent (I_{ph}), which is, therefore, particularly indicated to characterize the telecom performance of the ML laser. More specifically, we will refere to the averadge photocurrent defined as:

$$\overline{I}_{\text{ph}} = \frac{qV\mu_{\text{n}}}{h_{\text{SCH}}^2}\,\overline{n}_{\text{SCH}} \tag{3.16}$$

Again, it is possible to represent such parameter in a color map which gives a generic trends of the average photocurrent for each pair of bias condition (V-I).

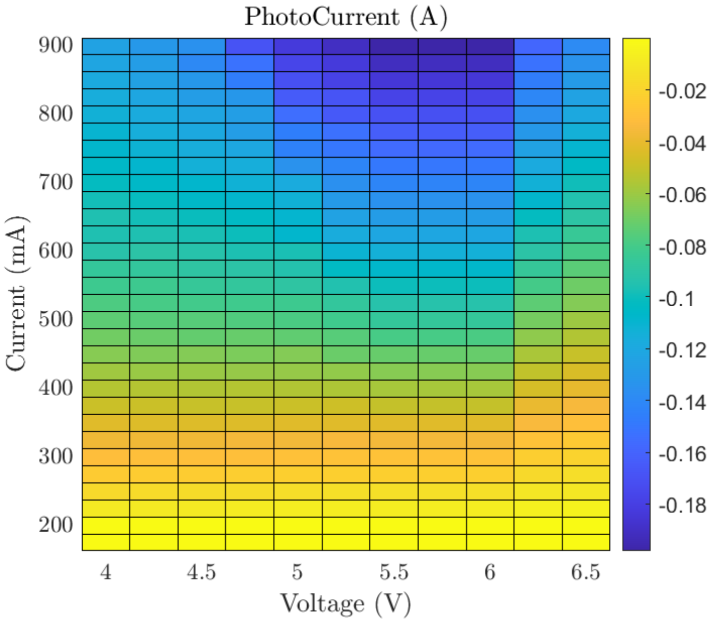

Figure 3.11: Map of the extracted average photocurrent

We notice that the values are negative because the SAs are inversely polarized. As is obvious, the largest values of photocurrents correspond to devices in which the gain sections are fed up with higher currents. However, comparing the Figures 3.7 and 3.11 it is possible to notice that the majority of the regions at higher photocurrent do not fulfill the stability condition or do not allow the circulation of 8 pulses. When a particular bias configuration is chosen, it is possible not only to calculate the extracted average photocurrent, but also to visualize its time evolution over the fundamental period. In this case, the extracted average photocurrent is $-114.4\,\text{mA}$. However, with respect to the time evolution of I_{ph}, a passband filter is applied to reshape the signal.

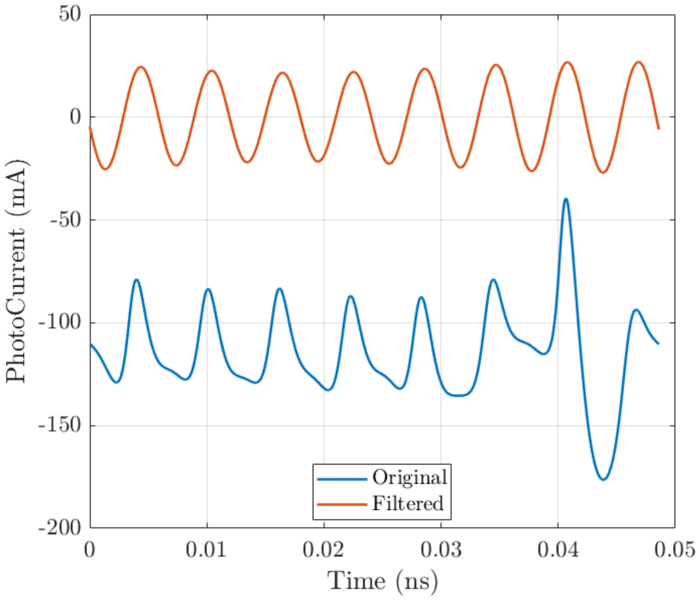

Figure 3.12: Trends of the Photocurrent extracted by the laser (in blue) and the one of the photocurrent subjected to the filtering pass band effect.

In Figure 3.12 it can be seen that the extracted signal is modulated in such a way as to appear nearly perfectly sinusoidal with a peak-peak amplitude of nearly 53.88 mA. Another figure of merit which can be computed is the filtering effect at which the extracted signal is subjected. To evaluate this parameter, we can give the following definition.

Definition 4 *The average effective original photocurrent is defined as the effective difference between the original photocurrent and its average value.*

This definition leads to the following mathematical expression:

$$\overline{I}_{\text{ph,eff}}^{\text{orig}} = eff\{I_{\text{ph}}^{\text{orig}} - \overline{I}_{\text{ph}}^{\text{orig}}\} \tag{3.17}$$

where $eff\{\cdot\}$ denotes the effective operator. In particular, the effective value of a signal $x(t)$ is defined as:

$$eff\{x(t)\} = \sqrt{\frac{1}{T}\int_0^T [x(t)]^2 \, dt} \tag{3.18}$$

For the previous bias point, it was estimated to be 22.31 mA. At this point, the aforementioned efficiency could be computed by calculating the ratio between the mean of the filtered photocurrent and the $\overline{I}_{\text{ph,eff}}^{\text{orig}}$. This turns out to be almost 77%. Finally, we present a discussion on the extracted pulse average and peak power.

The general map of these quantities, analyzed at the aforementioned bias point, are illustrated in Figures 3.13 and 3.14. In agreement with the photocurrent trends in the figure 3.11, the extracted power is higher for higher injection current values. However, both graphics show that the higher power is obtained for low voltage value. This is explainable taking advantage of the repetition rate illustration (figure 3.7) from which it is clear that the regions of higher power are also the ones in which there are fewer pulses. The basic affect is the distribution of the power on each pulse according to the conservation energy principle. Therefore, when there are few pulses, each one will carry more energy. On the other hand, the more pulses there are, the less energetic they will be.

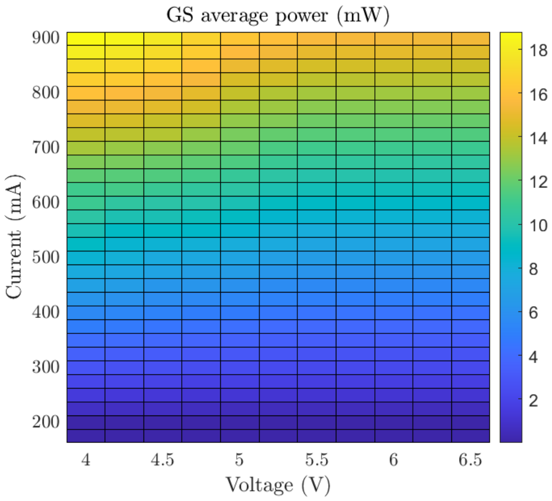

Figure 3.13: Average extracted power of a 16 sections QD-MLL.

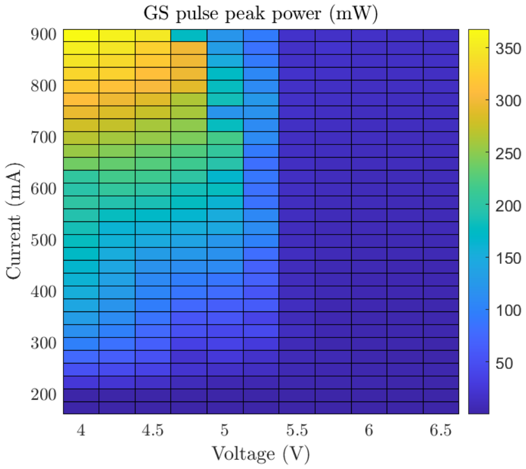

Figure 3.14: Peak of extracted power of a 16 sections QD-MLL.

Another noticeable characteristic is the fact that the average power is in general less intense than the corresponding peak one. This is due to the energetic nature on the pulses, indeed the power is zero for most of the period reducing the mean value. For the already quoted point A (Figure 3.7) their value are nearly 8.86 mW and 14.02 mW.

3.4 Comparative Analysis on a Device with 8 Sections

Once the basic behaviour and influence of each optical variable, their changes under different 8-section configuration was investigated. In particular, what is here presented is how the above stated results change when the ratio between the length of SAs and the total length of the cavity is increased. In the following analysis, a constant voltage of $-6\,\mathrm{V}$ was imposed to the SAs and the main figures of merit were registered the for the current condition which maximises them contemporaneously.

3.4.1 Peak-Peak Current and Effective Filered Photocurrent

The first subject of our study was the peak-peak amplitude of the filtered photocurrent, parameter that in the future will be indicated as I_{pp}. In Figure 3.15 it can be noticed that the behaviour of I_{pp} presents of three regimes. In the first one the peak-peak current is almost constant a part from some weak fluctuations. This indicates that, even if the dimension of the SAs increases, the amplitude of the extracted current does not vary in an appriciable way. Then a threshold zone is reached and in this case the peak-peak current increases very quickly until a maximum value. After that, the length of the saturable absorbers is too long and all the pulses are extinguished. This behaviour is also confirmed by the graphic of the effective filtered photocurrent which identifies the same threshold.

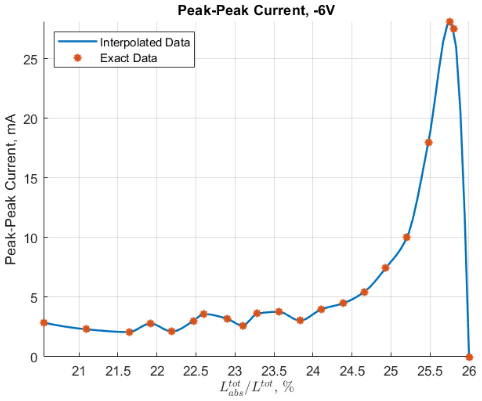

Figure 3.15: Peak-peak amplitude as a function of the ratio between the length of the SAs and the total length of the cavity.

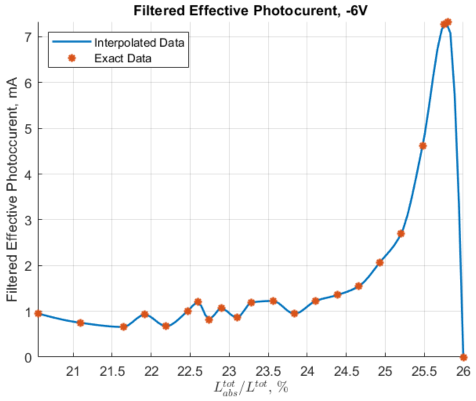

Figure 3.16: Effective mean photocurrent as a function of the ratio between the length of the SAs and the total length of the cavity.

3.4.2 Filtering Efficiency

Another figure of merit is the filtering efficiency, which is the percentage of original effective photocurrent that is filtered. In Section 3.3.2 it was calculated for a single bias point; now it was registered and plotted for different devices at a constant voltage. The main results are shown in the Figure 3.17 which clearly demonstrates a decreasing function of the ratio between the length of the SAs and the one of the total cavity. In other words, the filtering effect of the unwanted RF component to transmit a sinusoidal signal is becoming more and more relevant as the aforementioned ratio increases. The decreasing trend of such a parameter is due to the fact that the total original extracted photocurrent increases as the aforementioned ratio increases, but less and less filtered photocurrent is present. When these results are compared with the trends of the peak-peak amplitude and the effective current, it is straightforward to notice the trade-off between the filtering efficiency and the photocurrent. Indeed, for configurations with high $I_{\mathrm{ph}}^{\mathrm{fil}}$, there is low filtering efficiency and vice versa. However, in such situations, the filtering efficiency is not low enough to compromise the presence of a peak (Figures 3.15 and 3.16).

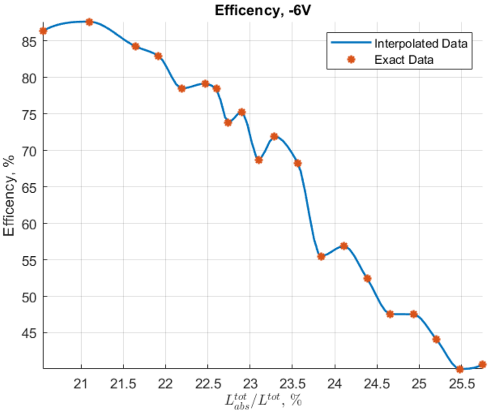

Figure 3.17: Filtering efficiency when $V = -6\,\mathrm{V}$ in a 8-section MLL

3.5 Simulation of alternative structures

As illustrated in the previous section, there is a high tenability of the geometrical parameters. Therefore, to increase the repetition frequency, structures with a higher number of sections were also simulated. The results of the simulations of devices with 18 and 20 sections are reported here.

3.5.1 18-section devices

As discussed above, by changing the number of sections it is possible to achieve a higher repetition rate with a longer cavity. Our first aim was to simulate a device of 18 sections operating at the same repetition frequency as the device of 16 sections aforementioned.

Repetition frequency equal to 165 GHz

The first step for the simulation of an 18-section device with a repetition frequency of 165 GHz is the calculation of the corresponding cavity length. Taking advantage

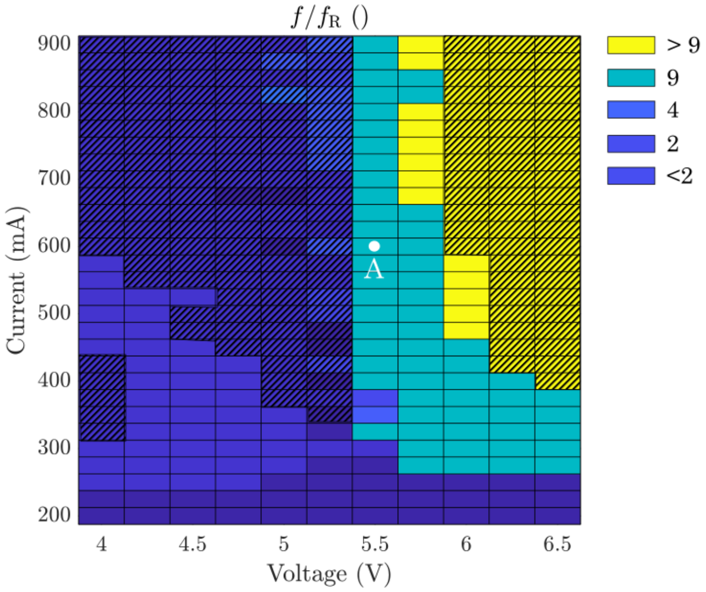

Figure 3.18: Map of the ratio between the repetition rate and the fundamental frequency in the case of a 18 section device. The instabilities regions are highlighted with oblique lines.

of the equation (3.13), it is possible to state that:

$$L = \frac{N_S\ c}{2n_r f} \tag{3.19}$$

In this case, we chose to maintain constant the sum of the length of gain and absorber sections so that the total length of the cavity results to be nearly equal to 4470.94 µm. In turn, the fundamental harmonic is easily calculated as follows:

$$f_R = \frac{f}{9} = 18.33\,\mathrm{GHz} \tag{3.20}$$

The map of the repetition frequency divided by the fundamental one is represented in Figure 3.18. As can be seen, the dimensions of the instability region are comparable to those in the previous case. Again, it is possible to choose a particular bias condition to visualize the behavior of pulses in the time and frequency domain (Figures 3.19 and 3.20).

The confirmation that the 18-section device works at a repetition frequency of the 165 GHz is the fact that the ninth harmonic is the predominant one in the RF spectrum. Regarding the average photocurrent, the map which analyzes this parameter in all the bias windows is depicted in Figure 3.21. Again, it is possible to see how the highest vales of the average photocurrent are obtained for high values of voltage and current, but unfortunately, these conditions are characterized by instability.

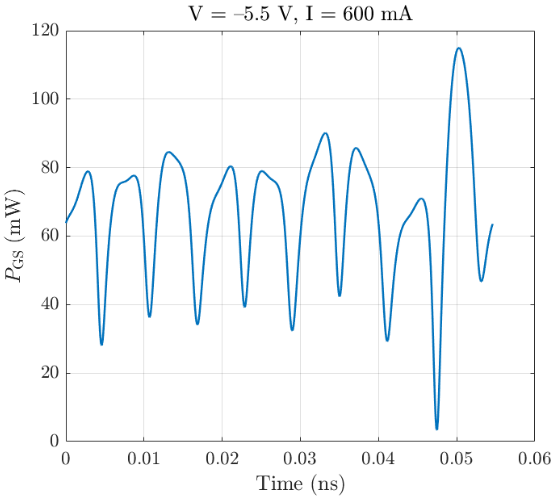

Figure 3.19: 9 pulses in time domain when a current of 600 mA is injected in the gain sections and the saturable absorbers are biased with a voltage of -5.5 V.

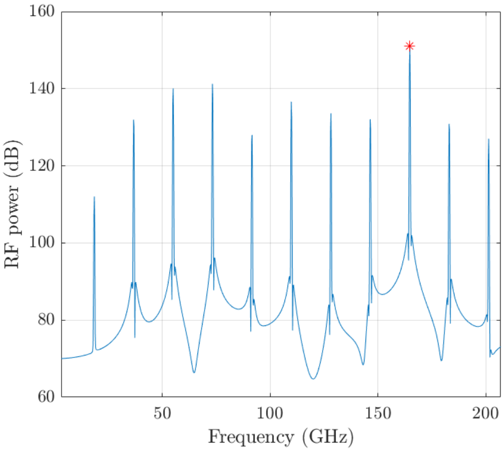

Figure 3.20: RF spectrum of the signal when a current of 600 mA is injected in the gain sections and the saturable absorbers are biased with a voltage of -5.5 V.

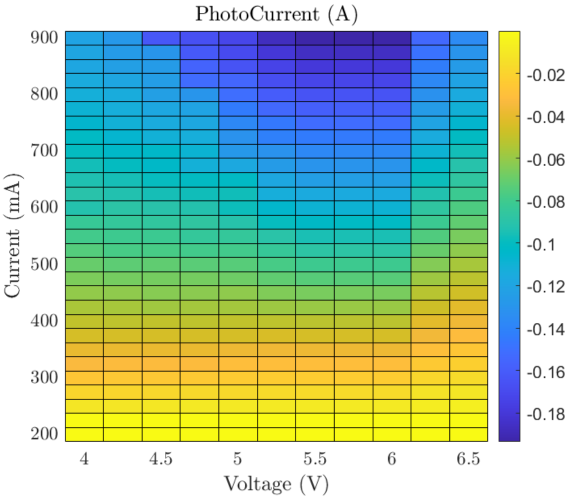

Figure 3.21: Map of the extracted average photocurrent

This confirms the trade-off between stability and average photocurrent. In this case, the configuration with $V = -5.5\,\mathrm{V}$, $I = 600\,\mathrm{mA}$, is capable of producing an average extracted photocurrent of $-109.3\,\mathrm{mA}$. It can be seen that this parameter remained almost equal to the one calculated for the 16 section device (with a slight variation of nearly 4%). The time evolution of the photocurrent is illustrated in Figure 3.22.

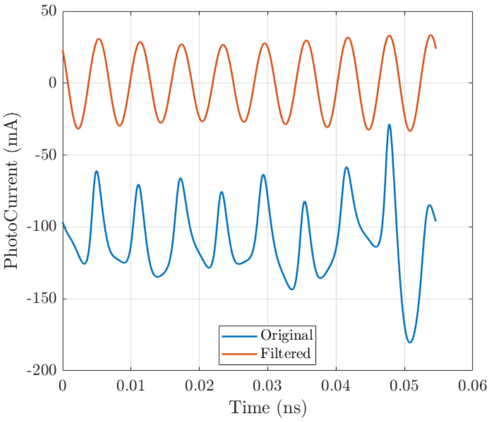

Figure 3.22: Trends of the photocurrent extracted by the laser (in blue) and the one of the photocurrent subjected to the filtering pass band effect.

It is noticeable that, in this case, the peak-peak amplitude is nearly 56.31 mA which is a value close to the one computed for the 16-section device (with a coherent variation of 4%). The filtering efficiency is also nearly constant since, in this case, it is computed to be 79% (with a little improvement of 4%). Regarding the extracted power, the maps of its average and maximum values are reported in the Figures 3.23 and 3.24 where the highest values of such parameters are again obtained in the bias condition of low voltages and high currents.

In point A, the average and maximum power are, respectively, 7.49 mW and 12.80 mW. Inherently with the principle of the conservation of energy, the presence of more pulses in the cavity will induce lower power values with respect to the ones computed for the 16-section device.

Repetition frequency of 150 GHz

In order to illustrate a comparative analysis between different devices, also 18 sections MLL operating at a repetition frequency of 150 GHz was designed. Taking advantage of the equation (3.13) it is possible to calculate the total length cavity as:

$$L = \frac{N_S\, c}{2 n_r f} = 4918\,\mu\mathrm{m} \tag{3.21}$$

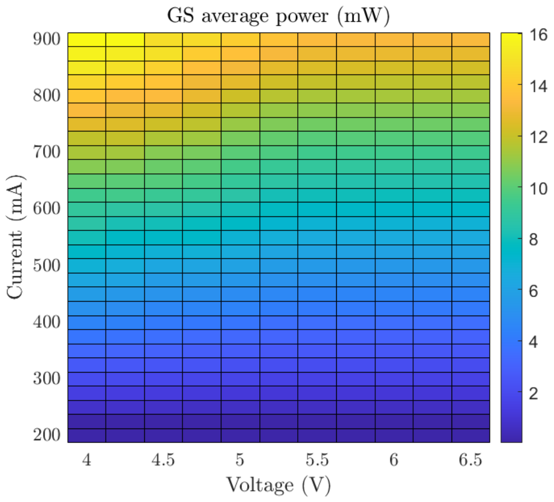

Figure 3.23: Average extracted power of a 18 sections QD-MLL.

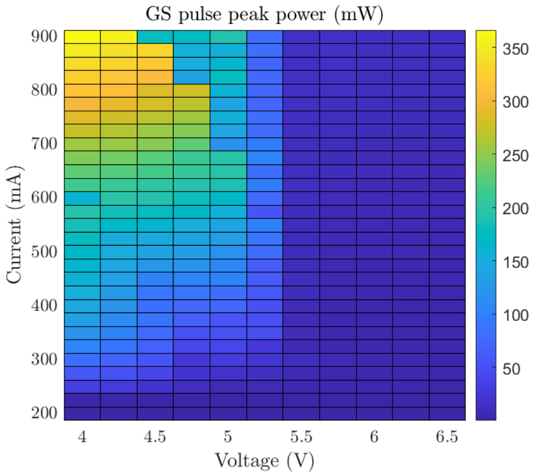

Figure 3.24: Peak of extracted power of a 18 sections QD-MLL.

In this case the fundamental frequency is estimated to be:

$$f_R = \frac{f}{9} = 16.67\,\text{GHz} \tag{3.22}$$

and the sum of a single SA and gain section is:

$$L_{\text{abs}} + L_{\text{gain}} = \frac{L}{9} = 546.45\,\mu\text{m} \tag{3.23}$$

The map of the bias conditions for which 9 stable pulses circulates in the cavity is illustrated in the Figure 3.25.

Figure 3.25 clearly shows a wider stability region compared to the device of the previous 18-section device with more bias conditions that can reach a steady-state regime. Concerning the representation of pulses in the time and frequency domains, their trends are shown in Figures 3.26 and 3.27.

The Figure 3.26 shows 9 net pulses with fewer instabilities than in the previous cases. Again, a further confirmation that the device is operating with the requested repetition frequency in this specific bias condition is the fact that the ninth harmonic in the RF spectrum is in correspondence of 150 GHz and it is the predominant component of the spectrum. Another figure of merit is the general behavior of the average photocurrent, which is reported in Figure 3.28.

In this case, a higher average photocurrent is obtained for high voltage and current values, confirming once again the trade-off between stability (illustrated in Figure 3.25) and $\overline{I}_{\text{ph}}$. The specific time evolution of the extracted photocurrent is depicted in the Figure 3.29. In this case, $\overline{I}_{\text{ph}} = -104.2\,\text{mA}$ (with a reduction of almost 4% compared to the case of the 18-section device operating at 165 GHz) and

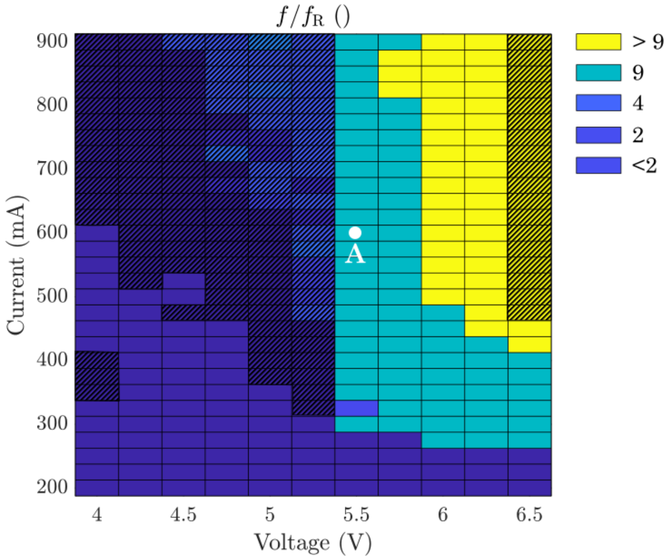

Figure 3.25: Map of the ratio between the repetition rate and the fundamental frequency. The instabilities regions are highlighted with oblique lines.

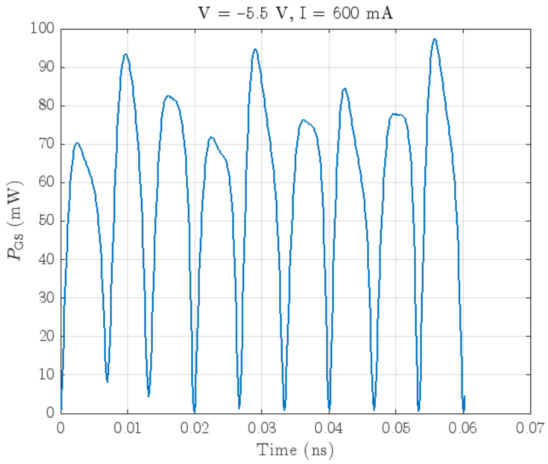

Figure 3.26: 9 pulses in time domain when in the gain section it is injected a current of 600 mA and the saturable absorbers are biased with a voltage of −5.5 V.

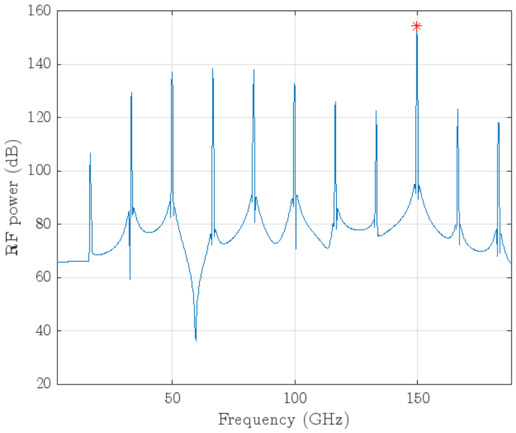

Figure 3.27: RF spectrum of the signal when in the gain section it is injected a current of 600 mA and the saturable absorbers are biased with a voltage of −5.5 V.

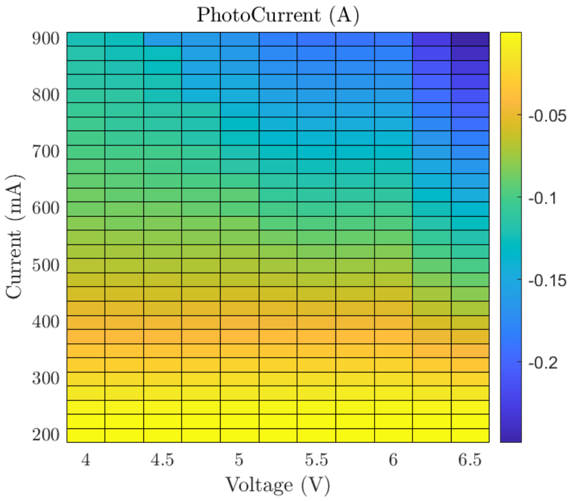

Figure 3.28: Map of the extracted average photocurrent as calculated in the equation (3.16).

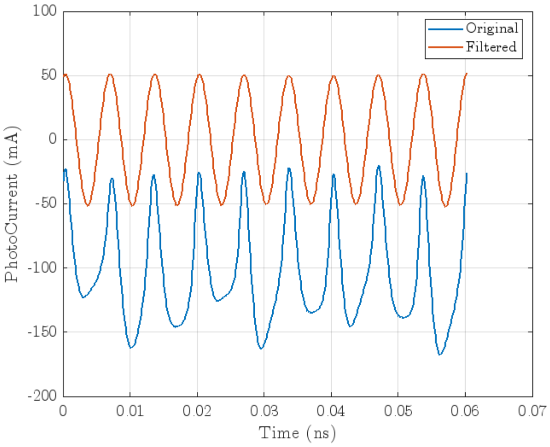

Figure 3.29: Trends of the extracted original (in blue) and filtered (in red) photocurrent.

a peak-to-peak amplitude that is much higher than in the previous case, estimated as 104.49 mA (nearly double of the peak-peak amplitude associated to the device in the previous paragraph). Filtering efficiency is also improved now: It is estimated to be near 89%. Regarding the behavior of the extracted power, it is described in Figures 3.30 and 3.31.

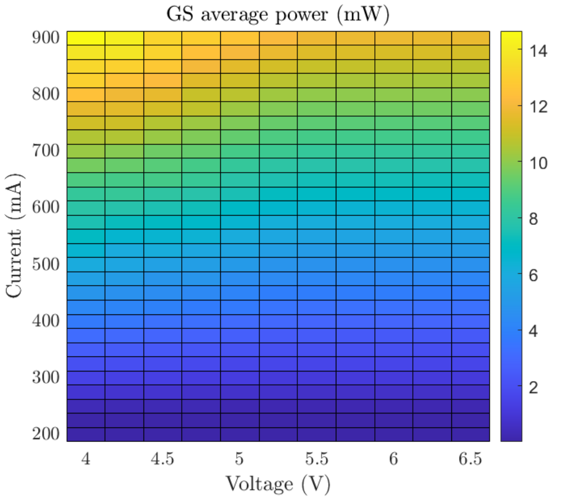

Figure 3.30: Average extracted power of a 18 sections QD-MLL.

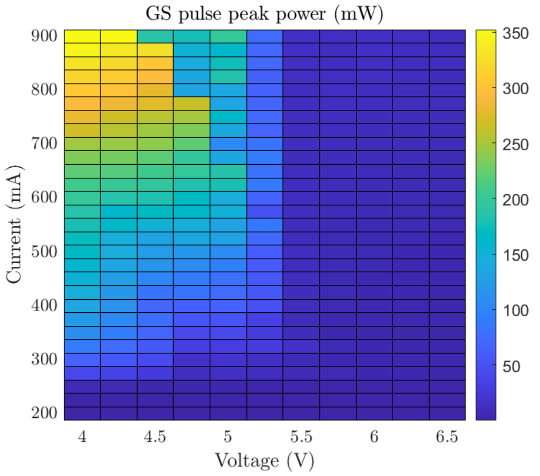

Figure 3.31: Peak of extracted power of a 18 sections QD-MLL.

Again, it is possible to recognize high-power values for low voltages and high current. When considering the average and maximum extracted power for the configuration at point A, it is noticeable that $P_{\text{avg}} = 6.48\,\text{mW}$ and $P_{\text{max}} = 11.19\,\text{mW}$. It is remarkable how these values are nearly 13% lower than the respective values in the 18-section device operating at 165 GHz.

3.6 Final remarks

In the previous paragraphs, the possibility of using a QD-based mode locking laser as a signal source for RF transmission has been demonstrated. The main figures of merit of the 16- and 18-section devices with repetition frequencies of 165 GHz and 150 GHz have been discussed, focusing on the stability of the pulses and the performance of the extracted signals. In particular, we have highlighted that the 150 GHz-working device based on 18 sections has a better response in terms of filtering efficiency and pulse stability. This last characteristic is the most critical point to take into account when designing a laser cavity capable of maintaining frequency repetition rates above 165 GHz. Indeed,the trade-off between stability and high frequency repetition rate is particularly relevant especially at high frequency. Attempts have been made to project cavities able to sustain $f = 180\,\text{GHz}$ but it was impossible to achieve steady-state operations. This allowed us to conclude that, according to our model, the type of QDs we considered cannot sustain these large repetition frequencies. Moreover, other effects, such as the dynamic effects of holes, should be included to complete the model. However, this topic remains one of the most researched and published topics in the literature, and therefore it is reasonable to affirm that other solutions will be developed to allow sub-terahertz transmission in a more stable way.

Chapter 4

Conclusions

This research activity was focused on the demonstration of the possibility to use the peculiar features of the Quantum Dots in order to sustain a repetition frequency above 150 GHz in ring lasers.

To this aim, the generic theory of lasers was given in Chapters 1 and 2, with particular attention to the model used to simulate the dynamic effect which occurs in the lasing cavity. Practically, a pre-existing MATLAB code was used, developed in the research group that hosted this thesis activity, and based on a delayed differential equation-based model describing the evolution of photons in the cavity. Initial efforts were made to fully understand the functionalities of such a program, which was revealed to be very flexible.

Geometrical and optical parameters were investigated to obtain a stable mode-locking condition that was able to work in the requested frequency range. After that, the program was re-adapted to simulate different geometrical configurations, in which the ratio between the length of the absorbers and the total length was varied. The results of such an analysis are reported in Chapter 3. In this part of the thesis, the results of the most significant configurations are also illustrated, presenting the main comparison between one device and the others. Additional efforts were made to identify the interdependence between the difference parameters. The provided MS-DDE model demonstrated to be a practical tool in the very preliminary stages for telecommunications applications. Indeed, the natural employment of what was analyzed is the use of QD mode-locking laser as a signal source for the future 5G and 6G transmissions. In Chapter 3 it is also illustrated one possible example of an antenna to be employed for such a purpose.

Of particular relevance are the results obtained in terms of the filtered photocurrent peak-peak amplitude and efficiency. In fact, in a 18-section device designed to have a repetition rate of 150 GHz, wide stable operating conditions have been demonstrated. As a proof of the good performance of this device, the filtered photocurrent was analyzed, exhibiting a peak-peak amplitude in (−5.5 V, 600 mA) of 104.49 mA and a filtering efficiency of 89%. Lasers characterized by a repetition frequency of 165 GHz are also reported, but they suffer of more instability phenomena even if their performances in terms of peak-peak amplitude photocurrent and filtering efficiency are appreciable. The first device based on the 16-section is characterized, in the aforementioned bias conditions, by a peak-peak amplitude of 53.88 mA with a filtering efficiency of 77%. Similar results has been found analysing a 18 section-based device working at the same repetion rate.

Finally, stable pulses at high repetition frequency seem to be impossible. This is due to the instability effect, which becomes relevant in such regime. Probably, other solutions will be studied in the future to take advantage of this promising technology.

Future works include the improvements of the code to optimize it and include additional effects, such as the non-exitonic interaction.

Appendix A

MATLAB Codes

A.1 16 Sections Ring Lasers (165GHz)

```
% Geometry
% 'Ring' -> ring laser, 'FP' -> Fabry-Perot laser
data.CavityType='Ring';
% Section lengths (um) Positive -> active section, negative -> absorption section
data.Lengths=[139 -87 278 -87 278 -87 278 -87 278 -87 278 -87 278 -87 278 -87 139]*(1.36);
% Number of slices used to divide the sections
data.Slices=[4,2,8,2,8,2,8,2,8,2,8,2,8,2,8,2,4];
% Waveguide width (um) (function of z or scalar)
data.Func_d=6;
% External cavity
% Include external cavity effect
data.IncludeExternalCavity=false;
% External cavity length (um)
data.Lec=0;
% External cavity losses (cm^-1)
data.alfai_ec=0;
% Confinement factors
% Confinement factor in the transversal direction (y) (function of z or scalar)
data.Func_gamma_trasv=0.75;
% Confinement factor in the vertical direction (x) (function of z or scalar)
data.Func_gamma_x=0.1;
% Reflectivities - Ring structure
```

```
% In a Ring configuration, only K_Laser is present,
    indicating  the amount of power that remains in the
    device
% 10% of the power is extracted, 90% remains in the
    cavity ()
data.K_Laser=0.9;                                   %
    Reflectivities - FP structure
% In a FP laser, the two facets reflectivities must be
    provided, while K_Laser is determined according to the
     chosen output facet

% External cavity
% Power external reflectivity ()
data.kec=0;                                         % Phase
    of the external reflectivity ()           data.phi_ec
    =0;                                     % Number of
    extra round trips in the external cavity ()
data.NumDelays=0;
% Losses
% Include losses
data.Func_alfai=1.5;
% Power intrinsic waveguide losses (cm^-1) (function of z
     or scalar)
data.IncludeLosses=true;

% Self Phase Modulation
data.IncludeSPM=0.2;

    % Self Phase Modulation effect scaling factor (0 ->
    not included)
% Spontaneous Emission
data.IncludeSpontEmissions=false;
                                                  % Include
    spontaneous emission noise
data.Dsp=1e-8;

    % Normalized spontaneous emission coefficient
% Spontaneous emission coefficient is automatically
    computed.
% However, it is possible to force an arbitrary value as
    follows.
```

```
% data.Bsp=1e-5;

   % Coupling coefficient spontaneous recombination ()
data.Bsp=0;

   % Einstein coefficient spontaneous recombination from
   WL (cm^3s^-1)
% Tunneling effect
data.eps_tunnelingWELL=1.2;
                                                    %
   Electron tunneling in WL %EG: controllare formula e
   udm
data.eps_tunnelingDOT=1.2;
                                                     %
   Electron tunneling in QD ()
% Other parameters
% Effective refractive index ()
data.nr=3.66;                                     %
   Internal quantum efficiency ()
data.etai=0.85;
% Global parameters
% Temperature (K)
data.T=293;                                       % Number
    of dot layers ()
data.NumLayers=12;                                % Dot
   surface radius (um)
data.Rdots=15.5e-3;
data.Vbi=-0.8;

   % Built-in voltage (V)
% Heights
data.H_QD=5e-3;

   % Dot layer height (um)
data.H_WL=7e-3;

   % Wetting Layer height (um)
data.H_SCH=180e-3;

   % Separate Confinement Heterostructure height (um)
% Electron effective masses
```

```
data.me_QD=0.02*9.11e-31;                                             % Electron effective mass in QD (kg)
data.me_WL=0.02*9.11e-31;                                             % Electron effective mass in WL (kg)
data.me_SCH=0.067*9.11e-31;                                           % Electron effective mass in SCH (kg)

%% QD physical parameters
% Time constants
data.tnr=[1;1;1e50;1e50;1e50];
data.tc=[0.2;0.2;0.2;0.2]*1e-3*3/3;                                   % Capture time in CB (ns)
data.tsp=[2.8;2.8;2.8];                                               % Spontaneous recombination time in CB (ns)
% Energy levels
data.Degeneracy=[6;4;2];                                              % Degeneracy in CB ()
data.Nd=2.85e2;                                                       % QD density (um^-2)
data.NumES=2;                                                         % Number of excited states considered in CB ()
data.E=[1.106;1.0597; 0.9986];                                        % Energy levels ES2, ES1, GS (eV)
data.WLenergygap=1.1539;                                              % WL energy gap (eV)
data.SCHenergygap=1.2797;                                             % SCH energy gap (eV)
data.DeltaE=[(data.SCHenergygap-data.WLenergygap)*0.7;...             % Energy difference between CB levels (eV)
    (data.WLenergygap-data.E(1))*0.77;-diff(data.E)];
```

```
%Bandwidth parameters:
data.BWhomogeneous_GS=25.751e3*34/34;                    % Inhomogeneous broadening single side HWHM (34 meV)
data.BWhomogeneous_ES=25.751e3*34/34;                    % Inhomogeneous broadening single side HWHM (34 meV)
% Auger recombination
data.tAu300K=[1e50;0.22*2.5;0.22*2.5;0.22]*3*0.75;       % Auger recombination time at T=300K (ns)
%data.tAu300K=data.tAu300K*0.75;
data.Ea=0.150;                                           % Temperature dependency of Auger coefficients (eV)
% Other parameters
%data.Gain=1.0539*(1.3*0.0533*[0.9292*0.508451668036196*1.031970836406555*1.00
%0.263308777919047*1.031957315692142*1.000002464495768]*1e-14);
data.Gain=[330;190];                                     % Gain (cm^-1)
data.PlasmaCoefficientvb=0*7.8e-18;                      % Plasma effect coefficient for VB(cm^2) [cost]
data.PlasmaCoefficient=0*7.8e-18;                        % Plasma effect coefficient for CB (cm^2) [cost]
data.enhanced_abs_sat_coeff=1.0;

%% Non-excitonic model
data.ExcitonicModel=true;                                % Excitonic model (false -> CB & VB solved separately)
data.tnrvb=[3;3;100;10;10;10;10];                        % Non-radiative recombination time in VB (ns)
data.tcvb=[7;7;7;7;7;7]*1e-3/10;                         % Capture
```

```
   time in CB (ns)
data.NumESvb=4;

   % Number of excited states considered in VB ()
data.DeltaEvb=[0.010;0.010;0.030;0.020;0.01730;0.01295];
                      % Energy difference between VB
   levels (eV)
data.Degeneracyvb=[6;6;6;4;2];
                                                 %
   Degeneracy in VB
% Hole effective masses
data.mh_QD=0.21*9.11e-31;
                                                      %
   Electron effective mass in QD (kg)
data.mh_WL=0.21*9.11e-31;
                                                      %
   Electron effective mass in WL (kg)
data.mh_SCH=0.47*9.11e-31;
                                                     %
   Electron effective mass in SCH (kg)
```

A.2 18 Sections Ring Laser (165 GHz)

```
% Geometry
% 'Ring' -> ring laser, 'FP' -> Fabry-Perot laser
data.CavityType='Ring';
data.Lengths=[139 -87 278 -87 278 -87 278 -87 278 -87 278
    -87 278 -87 278 -87 278 -87 139]*(1.36);
                         % Section lengths (um) Positive
   -> active section, negative -> absorption section
% Number of slices used to divide the sections

data.Slices=[4,2,8,2,8,2,8,2,8,2,8,2,8,2,8,2,8,2,4];
                                         % Waveguide
   width (um) (function of z or scalar)
% External cavity
data.Func_d=6;
% Include external cavity effect
data.IncludeExternalCavity=false;
% External cavity length (um)
data.Lec=0;
```

```
% External cavity losses (cm^-1)
data.alfai_ec=0;

% Confinement factors
% Confinement factor in the transversal direction (y) (function of z or scalar)
data.Func_gamma_trasv=0.75;
% Confinement factor in the vertical direction (x) (function of z or scalar)
data.Func_gamma_x=0.1;
% Reflectivities - Ring structure
% In a Ring configuration, only K_Laser is present, indicating  the amount of power that remains in the device
% 10% of the power is extracted, 90% remains in the cavity ()
data.K_Laser=0.9;
% Reflectivities - FP structure
% In a FP laser, the two facets reflectivities must be provided, while K_Laser is determined according to the chosen output facet
% Power reflectivity at the SA side
% data.Rleft=0.9;
% data.Rright=0.6;                              % Power reflectivity at the active side (possibly with EC)
% data.OutputFromRightFacet=true;               % The output is extracted from the right facet (gain side in the normal case of SA-G device)
% External cavity
data.kec=0;                                     % Power external reflectivity ()
data.phi_ec=0;                                  % Phase of the external reflectivity ()
data.NumDelays=0;                               % Number of extra round trips in the external cavity ()
```

```
% Losses
data.IncludeLosses=true;                                                    % Include losses
data.Func_alfai=1.5;                                                        % Power intrinsic waveguide losses (cm^-1) (function of z or scalar)
% Self Phase Modulation
data.IncludeSPM=0.2;                                                        % Self Phase Modulation effect scaling factor (0 -> not included)
% Spontaneous Emission
data.IncludeSpontEmissions=false;                                           % Include spontaneous emission noise
data.Dsp=1e-8;                                                              % Normalized spontaneous emission coefficient
% Spontaneous emission coefficient is automatically computed.
% However, it is possible to force an arbitrary value as follows.
% data.Bsp=1e-5;                                                            % Coupling coefficient spontaneous recombination ()
data.Bsp=0;                                                                 % Einstein coefficient spontaneous recombination from WL (cm^3s^-1)
% Tunneling effect
data.eps_tunnelingWELL=1.2;                                                 % Electron tunneling in WL %EG: controllare formula e udm
data.eps_tunnelingDOT=1.2;                                                  % Electron tunneling in QD ()
% Other parameters
data.nr=3.66;
```

```
   % Effective refractive index ()
data.etai=0.85;

   % Internal quantum efficiency ()

% Global parameters
data.T=293;

   % Temperature (K)
data.NumLayers=12;

   % Number of dot layers ()
data.Rdots=15.5e-3;

   % Dot surface radius (um)
data.Vbi=-0.8;

   % Built-in voltage (V)
% Heights
data.H_QD=5e-3;

   % Dot layer height (um)
data.H_WL=7e-3;

   % Wetting Layer height (um)
data.H_SCH=180e-3;

   % Separate Confinement Heterostructure height (um)
% Electron effective masses
data.me_QD=0.02*9.11e-31;
                                                                 %
   Electron effective mass in QD (kg)
data.me_WL=0.02*9.11e-31;
                                                                 %
   Electron effective mass in WL (kg)
data.me_SCH=0.067*9.11e-31;
                                                               %
   Electron effective mass in SCH (kg)

%% QD physical parameters
% Time constants
data.tnr=[1;1;1e50;1e50;1e50];
```

```
data.tc=[0.2;0.2;0.2;0.2]*1e-3*3/3;                                            % Capture time in CB (ns)
data.tsp=[2.8;2.8;2.8];                                                          % Spontaneous recombination time in CB (ns)
% Energy levels
data.Degeneracy=[6;4;2];                                                         % Degeneracy in CB ()
data.Nd=2.85e2;                                                                  % QD density (um^-2)
data.NumES=2;                                                                    % Number of excited states considered in CB ()
data.E=[1.106;1.0597; 0.9986];                                                   % Energy levels ES2, ES1, GS (eV)
data.WLenergygap=1.1539;                                                         % WL energy gap (eV)
data.SCHenergygap=1.2797;                                                        % SCH energy gap (eV)
data.DeltaE=[(data.SCHenergygap-data.WLenergygap)*0.7;...                        % Energy difference between CB levels (eV)
    (data.WLenergygap-data.E(1))*0.77;-diff(data.E)];
%Bandwidth parameters:
data.BWhomogeneous_GS=25.751e3*34/34;                                            % Inhomogeneous broadening single side HWHM (34 meV)
data.BWhomogeneous_ES=25.751e3*34/34;                                            % Inhomogeneous broadening single side HWHM (34 meV)
% Auger recombination
data.tAu300K=[1e50;0.22*2.5;0.22*2.5;0.22]*3*0.75;                              % Auger recombination time at T=300K (ns)
%data.tAu300K=data.tAu300K*0.75;
```

```
data.Ea=0.150;          % Temperature dependency of Auger coefficients (eV)
% Other parameters
%data.Gain= 1.0539*(1.3*0.0533*[0.9292*0.508451668036196*1.031970836406555*1.0
%  0.263308777919047*1.031957315692142*1.000002464495768]*1e-14);
data.Gain=[330;190];          % Gain (cm^-1)
data.PlasmaCoefficientvb=0*7.8e-18;                                  % Plasma effect coefficient for VB(cm^2) [cost]
data.PlasmaCoefficient=0*7.8e-18;                                     % Plasma effect coefficient for CB (cm^2) [cost]
data.enhanced_abs_sat_coeff=1.0;

%% Non-excitonic model
data.ExcitonicModel=true;                                                   % Excitonic model (false -> CB & VB solved separately)
data.tnrvb=[3;3;100;10;10;10;10];                                 % Non-radiative recombination time in VB (ns)
data.tcvb=[7;7;7;7;7;7]*1e-3/10;                                 % Capture time in CB (ns)
data.NumESvb=4;          % Number of excited states considered in VB ()
data.DeltaEvb=[0.010;0.010;0.030;0.020;0.01730;0.01295];              % Energy difference between VB levels (eV)
data.Degeneracyvb=[6;6;6;4;2];                                          % Degeneracy in VB
% Hole effective masses
```

```
data.mh_QD=0.21*9.11e-31;                                          % Electron effective mass in QD (kg)
data.mh_WL=0.21*9.11e-31;                                          % Electron effective mass in WL (kg)
data.mh_SCH=0.47*9.11e-31;                                         % Electron effective mass in SCH (kg)
```

A.3 18 Sections Ring Laser (150 GHz)

```
% Geometry
data.CavityType='Ring';                                            % 'Ring' -> ring laser, 'FP' -> Fabry-Perot laser
data.Lengths=[139 -87 278 -87 278 -87 278 -87 278 -87 278 -87 278 -87 278 -87 278 -87 139]*(1.497);                          % Section lengths (um) Positive -> active section, negative -> absorption section
data.Slices=[4,2,8,2,8,2,8,2,8,2,8,2,8,2,8,2,8,2,4];                          % Number of slices used to divide the sections
data.Func_d=6;                                                     % Waveguide width (um) (function of z or scalar)
% External cavity
data.IncludeExternalCavity=false;                                  % Include external cavity effect
data.Lec=0;                                                        % External cavity length (um)
data.alfai_ec=0;                                                   % External cavity losses (cm^-1)
% Confinement factors
data.Func_gamma_trasv=0.75;                                        % Confinement factor in the transversal direction (y) (function of z or scalar)
```

```
data.Func_gamma_x=0.1;                                        % Confinement factor in the vertical direction (x) (function of z or scalar)
% Reflectivities - Ring structure
% In a Ring configuration, only K_Laser is present, indicating  the amount of power that remains in the device
data.K_Laser=0.9;                                             % 10% of the power is extracted, 90% remains in the cavity ()
% Reflectivities - FP structure
% In a FP laser, the two facets reflectivities must be provided, while K_Laser is determined according to the chosen output facet
% data.Rleft=0.9;                                             % Power reflectivity at the SA side
% data.Rright=0.6;                                            % Power reflectivity at the active side (possibly with EC)
% data.OutputFromRightFacet=true;                             % The output is extracted from the right facet (gain side in the normal case of SA-G device)
% External cavity
data.kec=0;                                                   % Power external reflectivity ()
data.phi_ec=0;                                                % Phase of the external reflectivity ()
data.NumDelays=0;                                             % Number of extra round trips in the external cavity ()
% Losses
data.IncludeLosses=true;                                      % Include losses
```

```
data.Func_alfai=1.5;

    % Power intrinsic waveguide losses (cm^-1) (function
    of z or scalar)
% Self Phase Modulation
data.IncludeSPM=0.2;

    % Self Phase Modulation effect scaling factor (0 ->
    not included)
% Spontaneous Emission
data.IncludeSpontEmissions=false;
                                                       % Include
    spontaneous emission noise
data.Dsp=1e-8;

    % Normalized spontaneous emission coefficient
% Spontaneous emission coefficient is automatically
    computed.
% However, it is possible to force an arbitrary value as
    follows.
% data.Bsp=1e-5;

    % Coupling coefficient spontaneous recombination ()
data.Bsp=0;

    % Einstein coefficient spontaneous recombination from
    WL (cm^3s^-1)
% Tunneling effect
data.eps_tunnelingWELL=1.2;
                                                            %
    Electron tunneling in WL %EG: controllare formula e
    udm
data.eps_tunnelingDOT=1.2;
                                                             %
    Electron tunneling in QD ()
% Other parameters
data.nr=3.66;

    % Effective refractive index ()
data.etai=0.85;

    % Internal quantum efficiency ()
```

```

% Global parameters
data.T=293;                                  % Temperature (K)
data.NumLayers=12;                           % Number of dot layers ()
data.Rdots=15.5e-3;                          % Dot surface radius (um)
data.Vbi=-0.8;                               % Built-in voltage (V)
% Heights
data.H_QD=5e-3;                              % Dot layer height (um)
data.H_WL=7e-3;                              % Wetting Layer height (um)
data.H_SCH=180e-3;                           % Separate Confinement Heterostructure height (um)
% Electron effective masses
data.me_QD=0.02*9.11e-31;                    % Electron effective mass in QD (kg)
data.me_WL=0.02*9.11e-31;                    % Electron effective mass in WL (kg)
data.me_SCH=0.067*9.11e-31;                  % Electron effective mass in SCH (kg)

%% QD physical parameters
% Time constants
data.tnr=[1;1;1e50;1e50;1e50];
data.tc=[0.2;0.2;0.2;0.2]*1e-3*3/3;          % Capture time in CB (ns)
```

```
data.tsp=[2.8;2.8;2.8];                                                  % Spontaneous recombination time in CB (ns)
% Energy levels
data.Degeneracy=[6;4;2];                                                 % Degeneracy in CB ()
data.Nd=2.85e2;                                                          % QD density (um^-2)
data.NumES=2;                                                            % Number of excited states considered in CB ()
data.E=[1.106;1.0597; 0.9986];                                           % Energy levels ES2, ES1, GS (eV)
data.WLenergygap=1.1539;                                                 % WL energy gap (eV)
data.SCHenergygap=1.2797;                                                % SCH energy gap (eV)
data.DeltaE=[(data.SCHenergygap-data.WLenergygap)*0.7;...                % Energy difference between CB levels (eV)
    (data.WLenergygap-data.E(1))*0.77;-diff(data.E)];
%Bandwidth parameters:
data.BWhomogeneous_GS=25.751e3*34/34;                                    % Inhomogeneous broadening single side HWHM (34 meV)
data.BWhomogeneous_ES=25.751e3*34/34;                                    % Inhomogeneous broadening single side HWHM (34 meV)
% Auger recombination
data.tAu300K=[1e50;0.22*2.5;0.22*2.5;0.22]*3*0.75;                       % Auger recombination time at T=300K (ns)
%data.tAu300K=data.tAu300K*0.75;
data.Ea=0.150;                                                           % Temperature dependency of Auger coefficients (eV)
% Other parameters
```

```
%data.Gain=1.0539*(1.3*0.0533*[0.9292*0.508451668036196*1.031970836406555*1.0
%0.263308777919047*1.031957315692142*1.000002464495768]*1e-14);
data.Gain=[330;190];                % Gain (cm^-1)
data.PlasmaCoefficientvb=0*7.8e-18;                 % Plasma effect coefficient for VB(cm^2) [cost]
data.PlasmaCoefficient=0*7.8e-18;                   % Plasma effect coefficient for CB (cm^2) [cost]
data.enhanced_abs_sat_coeff=1.0;

%% Non-excitonic model
data.ExcitonicModel=true;                           % Excitonic model (false -> CB & VB solved separately)
data.tnrvb=[3;3;100;10;10;10;10];                   % Non-radiative recombination time in VB (ns)
data.tcvb=[7;7;7;7;7;7]*1e-3/10;                    % Capture time in CB (ns)
data.NumESvb=4;                     % Number of excited states considered in VB ()
data.DeltaEvb=[0.010;0.010;0.030;0.020;0.01730;0.01295];        % Energy difference between VB levels (eV)
data.Degeneracyvb=[6;6;6;4;2];                      % Degeneracy in VB
% Hole effective masses
data.mh_QD=0.21*9.11e-31;                           % Electron effective mass in QD (kg)
data.mh_WL=0.21*9.11e-31;                           %
```

```
   Electron effective mass in WL (kg)
data.mh_SCH=0.47*9.11e-31;
                                                                        %
   Electron effective mass in SCH (kg)
```

Bibliography

[1] Kouichi Akahane et al. “High-frequency short-pulse generation with a highly stacked InAs quantum dot mode-locked laser diode”. In: *Japanese Journal of Applied Physics* 60.SB (2021), SBBH02.

[2] Zhores I Alferov. “Nobel Lecture: The double heterostructure concept and its applications in physics, electronics, and technology”. In: *Reviews of modern physics* 73.3 (2001), p. 767.

[3] Rostislav Arkhipov et al. “Hybrid Mode Locking in Semiconductor Lasers: Simulations, Analysis, and Experiments”. In: *IEEE Journal of Selected Topics in Quantum Electronics* 19.4 (2013), pp. 1100208–1100208. DOI: `10.1109/JSTQE.2012.2228633`.

[4] Neil W Ashcroft and N David Mermin. *Solid state physics*. Cengage Learning, 2022.

[5] P Bardella et al. “Mode locking in a tapered two-section quantum dot laser: design and experiment”. In: *Optics letters* 43.12 (2018), pp. 2827–2830.

[6] D Bimberg et al. “High speed nanophotonic devices based on quantum dots”. In: *physica status solidi (a)* 203.14 (2006), pp. 3523–3532.

[7] Dieter Bimberg, Matthias Kuntz, and Matthias Laemmlin. “Quantum dot photonic devices for lightwave communication”. In: *Applied Physics A* 80 (2005), pp. 1179–1182.

[8] Dieter Bimberg and Udo W Pohl. “Quantum dots: promises and accomplishments”. In: *Materials Today* 14.9 (2011), pp. 388–397.

[9] Christian TA Brown et al. “Compact laser-diode-based femtosecond sources”. In: *New Journal of Physics* 6.1 (2004), p. 175.

[10] Steven Cherry. “Edholm’s law of bandwidth”. In: *IEEE spectrum* 41.7 (2004), pp. 58–60.

[11] Weng W Chow and Stephan W Koch. “Theory of semiconductor quantum-dot laser dynamics”. In: *IEEE journal of quantum electronics* 41.4 (2005), pp. 495–505.

[12] Larry A Coldren, Scott W Corzine, and Milan L Mashanovitch. *Diode lasers and photonic integrated circuits*. John Wiley & Sons, 2012.

[13] M DiDomenico Jr. “Small-signal analysis of internal (coupling-type) modulation of lasers”. In: *Journal of Applied Physics* 35.10 (1964), pp. 2870–2876.

[14] Mario Dumont et al. “High-efficiency quantum dot lasers as comb sources for DWDM applications”. In: *Applied Sciences* 12.4 (2022), p. 1836.

[15] John Federici and Lothar Moeller. “Review of terahertz and subterahertz wireless communications”. In: *Journal of Applied Physics* 107.11 (2010).

[16] Giuseppe Giannuzzi and Paolo Bardella. “Semiconductor racetrack resonator coupled to an S-bent waveguide: Influence of the coupling coefficients on the unidirectional operation”. In: *IET Optoelectronics* 15.3 (2021), pp. 131–138.

[17] R Gordon Gould et al. “The LASER, light amplification by stimulated emission of radiation”. In: *The Ann Arbor conference on optical pumping, the University of Michigan*. Vol. 15. 128. 1959, p. 92.

[18] Emanuele Groppo. “Sub-Terahertz Emission in Quantum Dot Semiconductor Lasers: a Delayed Differential Equation Approach”. Politecnico di Torino, 2022.

[19] Emanuele Groppo and Paolo Bardella. “Sub-terahertz Emission in Multi-Section Quantum Dot Ring Lasers: A Delayed Differential Equations Approach”. In: *2022 Asia Communications and Photonics Conference (ACP)*. IEEE. 2022, pp. 1456–1459.

[20] Emanuele Groppo, Lorenzo Tunesi, and Paolo Bardella. “Delayed differential equation-based study of sub-terahertz emission in multi-section quantum dot ring lasers”. In: *Novel In-Plane Semiconductor Lasers XXII*. Vol. 12440. SPIE. 2023, pp. 192–197.

[21] A Gubenko et al. “High-power monolithic passively modelocked quantum-dot laser”. In: *Electronics Letters* 41.20 (2005), pp. 1124–1125.

[22] Herman A Haus. “Mode-locking of lasers”. In: *IEEE Journal of Selected Topics in Quantum Electronics* 6.6 (2000), pp. 1173–1185.

[23] Hermann A Haus. “Theory of mode locking with a fast saturable absorber”. In: *Journal of Applied Physics* 46.7 (1975), pp. 3049–3058.

[24] Xiaodong Huang et al. “Passive mode-locking in 1.3 μm two-section InAs quantum dot lasers”. In: *Applied Physics Letters* 78.19 (2001), pp. 2825–2827.

[25] Yi Huang, Yaochun Shen, and Jiayou Wang. “From terahertz imaging to terahertz wireless communications”. In: *Engineering* 22 (2023), pp. 106–124.

[26] E. Ippen and C. Shank. “Sub-picosecond, kilowatt pulses from a mode-locked CW dye laser”. In: *IEEE Journal of Quantum Electronics* 10.9 (1974), pp. 722–722. DOI: `10.1109/JQE.1974.1068270`.

[27] Ronald Kaiser and Bernd Huttl. “Monolithic 40-GHz mode-locked MQW DBR lasers for high-speed optical communication systems”. In: *IEEE Journal of Selected Topics in Quantum Electronics* 13.1 (2007), pp. 125–135.

[28] Dmitry Kazakov et al. “Defect-engineered ring laser harmonic frequency combs”. In: *Optica* 8.10 (2021), pp. 1277–1280.

[29] Ursula Keller and R Paschotta. *Ultrafast Lasers*. Springer, 2021.

[30] Charles Kittel. *Introduction to solid state physics*. John Wiley & sons, inc, 2005.

[31] Roger GMP Koumans and Raymond Van Roijen. “Theory for passive mode-locking in semiconductor laser structures including the effects of self-phase modulation, dispersion, and pulse collisions”. In: *IEEE Journal of Quantum Electronics* 32.3 (1996), pp. 478–492.

[32] Matthias Kuntz et al. “High-speed mode-locked quantum-dot lasers and optical amplifiers”. In: *Proceedings of the IEEE* 95.9 (2007), pp. 1767–1778.

[33] KY Lau. “Gain switching of semiconductor injection lasers”. In: *Applied physics letters* 52.4 (1988), pp. 257–259.

[34] Yan Li et al. “Harmonic mode-locking using the double interval technique in quantum dot lasers”. In: *Optics express* 18.14 (2010), pp. 14637–14643.

[35] C-Y Lin et al. “Compact optical generation of microwave signals using a monolithic quantum dot passively mode-locked laser”. In: *IEEE Photonics Journal* 1.4 (2009), pp. 236–244.

[36] C-Y Lin et al. “RF linewidth reduction in a quantum dot passively mode-locked laser subject to external optical feedback”. In: *Applied Physics Letters* 96.5 (2010).

[37] Guocheng Liu et al. “Mode-locking and noise characteristics of InAs/InP quantum dash/dot lasers”. In: *Journal of Lightwave Technology* (2023).

[38] Jiaren Liu et al. “Dual-wavelength 92.5 GHz self-mode-locked InP-based quantum dot laser”. In: *Optics letters* 33.15 (2008), pp. 1702–1704.

[39] S Liu et al. “490 fs pulse generation from passively mode-locked single section quantum dot laser directly grown on on-axis GaP/Si”. In: *Electronics Letters* 54.7 (2018), pp. 432–433.

[40] Songtao Liu et al. “High-channel-count 20 GHz passively mode-locked quantum dot laser directly grown on Si with 4.1 Tbit/s transmission capacity”. In: *Optica* 6.2 (2019), pp. 128–134.

[41] Songtao Liu et al. “Monolithic 9 GHz passively mode locked quantum dot lasers directly grown on on-axis (001) Si”. In: *Applied Physics Letters* 113.4 (2018).

[42] Xueming Liu and Meng Pang. “Revealing the buildup dynamics of harmonic mode-locking states in ultrafast lasers”. In: *Laser & Photonics Reviews* 13.9 (2019), p. 1800333.

[43] ZG Lu et al. "312-fs pulse generation from a passive C-band InAs/InP quantum dot mode-locked laser". In: *Optics Express* 16.14 (2008), pp. 10835–10840.

[44] ZG Lu et al. "An L-band monolithic InAs/InP quantum dot mode-locked laser with femtosecond pulses". In: *Optics Express* 17.16 (2009), pp. 13609–13614.

[45] ZG Lu et al. "High performance InAs/InP quantum dot 34.462-GHz C-band coherent comb laser module". In: *Optics express* 26.2 (2018), pp. 2160–2167.

[46] G New. "Pulse evolution in mode-locked quasi-continuous lasers". In: *IEEE Journal of Quantum Electronics* 10.2 (1974), pp. 115–124.

[47] Shujie Pan et al. "Quantum dot mode-locked frequency comb with ultra-stable 25.5 GHz spacing between 20° C and 120° C". In: *Photonics Research* 8.12 (2020), pp. 1937–1942.

[48] Radoslaw Piesiewicz et al. "Scattering analysis for the modeling of THz communication systems". In: *IEEE Transactions on Antennas and Propagation* 55.11 (2007), pp. 3002–3009.

[49] E Pliński. "Terahertz photomixer". In: *bulletin of the polish academy of sciences technical sciences* (2010), pp. 463–470.

[50] Jiale Qin et al. "Ultra-reliable quantum dot colliding pulse mode-locked laser as multi-wavelength source for integrated optical interconnects". In: *Optics Express* 32.6 (2024), pp. 9095–9104.

[51] Edik U Rafailov et al. "High-power picosecond and femtosecond pulse generation from a two-section mode-locked quantum-dot laser". In: *Applied Physics Letters* 87.8 (2005), p. 081107.

[52] Mattia Rossetti, Paolo Bardella, and Ivo Montrosset. "Modeling passive mode-locking in quantum dot lasers: A comparison between a finite-difference traveling-wave model and a delayed differential equation approach". In: *IEEE Journal of Quantum Electronics* 47.5 (2011), pp. 569–576.

[53] Mattia Rossetti, Paolo Bardella, and Ivo Montrosset. "Time-domain travelling-wave model for quantum dot passively mode-locked lasers". In: *IEEE Journal of Quantum Electronics* 47.2 (2011), pp. 139–150.

[54] Claude Rulliere et al. *Femtosecond laser pulses*. Springer, 2005.

[55] W. Seitz et al. "All-optical synchronization and mode locking of solid-state lasers with nonlinear semiconductor Fabry-Perot mirrors". In: *IEEE Journal of Selected Topics in Quantum Electronics* 9.4 (2003), pp. 1093–1101. DOI: `10.1109/JSTQE.2003.819100`.

[56] Chen Shang et al. "High-temperature reliable quantum-dot lasers on Si with misfit and threading dislocation filters". In: *Optica* 8.5 (2021), pp. 749–754.

[57] Ho-Jin Song and Tadao Nagatsuma. “Present and future of terahertz communications”. In: *IEEE transactions on terahertz science and technology* 1.1 (2011), pp. 256–263.

[58] Sudharsanan Srinivasan et al. “Reliability of hybrid silicon distributed feedback lasers”. In: *IEEE Journal of Selected Topics in Quantum Electronics* 19.4 (2013), pp. 1501305–1501305.

[59] Mark G Thompson et al. “InGaAs quantum-dot mode-locked laser diodes”. In: *IEEE Journal of Selected Topics in Quantum Electronics* 15.3 (2009), pp. 661–672.

[60] MG Thompson et al. “10 GHz hybrid modelocking of monolithic InGaAs quantum dot lasers”. In: *Electronics Letters* 39.15 (2003), p. 1.

[61] MG Thompson et al. “Colliding-pulse modelocked quantum dot lasers”. In: *Electron. Lett* 41.5 (2005), pp. 248–250.

[62] MG Thompson et al. “Transform-limited optical pulses from 18 GHz monolithic modelocked quantum dot lasers operating at˜ 1.3 μm”. In: *Electronics Letters* 40.5 (2004), p. 1.

[63] Evgeny A Viktorov et al. “Model for mode locking in quantum dot lasers”. In: *Applied physics letters* 88.20 (2006).

[64] Andrei G Vladimirov and Dmitry Turaev. “Model for passive mode locking in semiconductor lasers”. In: *Physical Review A* 72.3 (2005), p. 033808.

[65] Andrei G Vladimirov et al. “Dynamical regimes in a monolithic passively mode-locked quantum dot laser”. In: *JOSA B* 27.10 (2010), pp. 2102–2109.

[66] Feihu Wang et al. “Ultrafast response of harmonic modelocked THz lasers”. In: *Light: Science & Applications* 9.1 (2020), p. 51.

[67] Zi-Hao Wang et al. “InAs/GaAs quantum dot single-section mode-locked lasers on Si (001) with optical self-injection feedback”. In: *Optics Express* 29.2 (2021), pp. 674–683.

[68] Wenqi Wei et al. “Reliable InAs quantum dot lasers grown on patterned Si (001) substrate with embedded hollow structures assisted thermal stress relaxation”. In: *Journal of Physics D: Applied Physics* 55.40 (2022), p. 405105.

[69] Bo Yang et al. “Active mode-locking optoelectronic oscillator”. In: *Optics Express* 28.22 (2020), pp. 33220–33227.

[70] L Zhang et al. “Low timing jitter, 5 GHz optical pulses from monolithic two-section passively mode-locked 1250/1310 nm quantum dot lasers for high speed optical interconnects”. In: *Optical Fiber Communication Conference*. Optica Publishing Group. 2005, OWM4.